

1 **Sedimentology, petrography and early diagenesis of a**
2 **travertine-colluvium succession from Chusang (southern Tibet)**

3
4 Zhijun Wang^a, Michael C. Meyer^{a,*}, Dirk L. Hoffmann^b

5 ^a Institute of Geology, University of Innsbruck, Innrain 52, 6020 Innsbruck, Austria

6 ^b Department of Human Evolution, Max Planck Institute for Evolutionary Anthropology, D-04103

7 Leipzig, Germany

8 *Corresponding author (michael.meyer@uibk.ac.at)

9
10
11 **ABSTRACT**

12 The Chusang travertine is situated in southern Tibet at an altitude of ~4200 m asl. in a cold-arid, periglacial
13 environment and is characterized by interbedding of hydrothermal carbonate with colluvium. Here we present
14 sedimentological and petrographical data to elucidate the depositional environment and sedimentary processes
15 responsible for hydrothermal carbonate precipitation and early diagenetic alteration as well as clastic sediment
16 accumulation and provide initial ²³⁰Th/U ages to constrain the time-depth of this travertine-colluvium
17 succession. .

18 Three main travertine lithofacies have been identified: 1) a dense laminated lithofacies composed of thick
19 dendritic laminae alternating with thin micrite laminae, 2) a porous layered lithofacies consisting of cm-thick
20 highly porous and biologically mediated calcite layers alternating with dense calcite layers preserving relict
21 dendrites, 3) an intraclastic lithofacies that results from erosion of pre-existing hot spring carbonate. The
22 colluvium is composed of cohesive debris flow layers that derived from high-magnitude, low-frequency,
23 mass-wasting events from the adjacent hillslopes. Micro-fabric analyses suggest that dense laminated travertine
24 forms via rapid calcite precipitation from hot spring water seasonally subjected to severe winter cooling, while
25 porous layered travertine results from seasonal dilution of hot spring water with rain water during the summer
26 monsoon months, which in turn stimulates biological productivity and gives rise to a porous summer layer. Early
27 diagenesis in the form of recrystallization and extensive formation of pore cements is common in the Chusang
28 travertine, but never eradicates the original crystal fabrics completely.

29 The sedimentary architecture of the deposit is conditioned by (i) the gently dipping (~10°) pre-existing

30 terrain on which hot spring water is discharged from multiple travertine mounds causing laterally extensive
31 travertine sheets to precipitate, and (ii) the adjacent much steeper (up to 30°) periglacial hill slopes that are the
32 source area of repeated debris flows that accumulate on the travertine surface. The resulting travertine–colluvium
33 succession has a total thickness of ~24 m and ²³⁰Th/U dating suggest that the base of this succession has a
34 minimum age of ~486 ka, while the upper part (top-most ~8 m) of the succession started accumulating in the
35 earliest Holocene. We hypothesize that hot spring activity (and thus travertine precipitation) and the occurrence
36 of debris flow events have a climatic nexus, i.e. are both triggered by phases of enhanced Indian summer
37 monsoon.

38

39 Keywords: Tibetan Plateau; hydrothermal spring carbonate; travertine; colluvium; early diagenesis; monsoon

40

41

42 **1. Introduction**

43 Travertines are continental spring carbonates that precipitate from hydrothermal water
44 (generally >30°C in temperature) and that are typically bound to crustal-scale faults in extensional
45 tectonic regimes (Özkul et al., 2002; Zentmeyr et al., 2008; Capezzuoli et al., 2014; Della Porta, 2015;
46 Croci et al., 2016). High rates of carbonate precipitation are common in travertines (frequently ≥ 1
47 cm/year; Pentecost, 2005) with two major consequences: (i) rapid crystal growth that results in high
48 primary porosity, and (ii) high temporal resolution of proxy signals stored in these deposits. The latter
49 effect is often expressed as lamination that resolves climate and temperature variability on a seasonal
50 (Chafetz and Folk, 1984; Liu et al., 2010), and sometimes monthly or even diurnal scale (Chafetz and
51 Folk, 1984; Takashima and Kano, 2008). Furthermore, spring carbonates such as travertines are – at
52 least in principle – amenable to uranium-series disequilibrium dating (e.g. ²³⁰Th/U dating; Mallick and
53 Frank, 2002; Garnett et al., 2004; Stone et al., 2010) as well as luminescence dating (Rich et al., 2003;
54 Mahan et al., 2007; Vazquez-Urbez et al., 2011), and are hence valuable archives of paleoclimatic and
55 paleoenvironmental change (Frank et al., 2000; Minissale et al., 2002; Faccenna et al., 2008; Liu et al.,
56 2010; Toker et al., 2015). In several reported instances travertines as well as other types of continental
57 spring carbonates are also stratigraphically and/or spatially associated with archaeological remains,
58 especially in arid and semi-arid areas (the Tibetan highlands included) and can thus act as valuable

59 archaeological repositories too (Grün et al., 1998; Hill, 2001; Smith et al., 2004; 2007; Ashley et al.,
60 2010; Zhang and Li, 2002).

61 Exploiting the paleoenvironmental and geoarchaeological information stored in travertines is,
62 however, impeded by the fact that these deposits are prone to early diagenesis, because of their high
63 initial porosity and permeability (Pentecost, 2005; Jones and Renaut, 2010; Capezzuoli et al., 2014).
64 Diagenesis can alter the geochemical composition and thus paleoclimatic proxy signals recorded in
65 spring carbonate deposits (Andrews, 2006), and also cause problems for $^{230}\text{Th}/\text{U}$ dating (e.g.
66 open-system behavior with respect to Uranium and/or Thorium; Garnett et al., 2004; Stone et al.,
67 2010). Moreover, detrital material (e.g. clay minerals) might afflict the quality of $^{230}\text{Th}/\text{U}$ dates of
68 these deposits. Hence, a detailed study of the macroscopic and microscopic crystal fabrics and
69 reconstruction of the depositional environments is necessary to gain insights into the sedimentary and
70 diagenetic history of travertines (Chafetz and Folk, 1984; Jones and Renaut, 2008; Rainey and Jones,
71 2009) and to assess their fidelity as a paleoenvironmental archive.

72 On the Tibetan plateau, hydrothermal springs and travertine deposits are common and
73 preferentially occur along north-south trending active graben systems (Tong et al., 2000). Yet, in a
74 Tibetan context, these hydrothermal spring carbonates are severely under-researched. Little is known
75 about the nature of paleoclimatic information stored in these carbonates and the paleoenvironmental
76 significance of past periods of travertine formation. The few Tibetan travertine sites that have been
77 described so far include the Targjia and the Zabuye travertine (both central Tibet; Zhao et al., 2006;
78 Zhao et al., 2010), the Nyalam travertine (southern Tibet; Zentmyer et al., 2008) and the Rongma
79 travertine (northern Tibet; Gao et al., 2013). One particularly interesting travertine site is situated ca.
80 80 km northwest of Lhasa (Chusang; Fig. 1), where nineteen human hand- and footprints were
81 discovered on the surface of the Chusang travertine (Zhang and Li, 2002), and are thought to be of
82 Late Pleistocene age (Zhang and Li, 2002; Zhang et al., 2003), rendering Chusang an archaeological
83 key site for the Tibetan plateau. Furthermore, the travertine deposit at Chusang is interbedded with
84 colluvium and alluvium resulting in a ~24 m thick succession of hydrothermal carbonate and detrital
85 terrigenous strata. Only very few examples of such mixed travertine-terrigenous successions have
86 been described so far (e.g. Schulte et al., 2008; Zentmeyr et al., 2008; Claes et al., 2014; Özkul et al.,
87 2014; Croci et al., 2016), but these studies already highlight the variety of lithofacies types and
88 different depositional architectures encountered in these deposits.

89 Alluvial fans and colluvial deposits are common on the Tibetan plateau, owing to the sparse
90 vegetation cover and periglacial processes operating on the hill slopes. Nevertheless, these
91 unconsolidated sediments are also highly erodible; hence most of these terrigenous deposits reflect the
92 latest Pleistocene and Holocene sedimentary dynamics on the plateau only (Wang and French, 1995;
93 Kaiser et al., 2007, 2009). In the case of Chusang, however, the travertine layers are shielding the
94 interbedded colluvial strata from erosion, and it is thus likely that in the stratigraphically lower part of
95 the succession much older colluvium is preserved as compared to the adjacent hillslopes, allowing
96 sediment based climate records to be extended back in time.

97 In this study, we conducted sedimentological and petrographic analyses on the
98 travertine-colluvium succession of Chusang in order to reconstruct its stratigraphic architecture and
99 depositional environment, to elucidate the processes responsible for travertine precipitation and to
100 investigate the degree of diagenetic alteration. This work thus (i) lays the foundation for a $^{230}\text{Th}/\text{U}$
101 dating study, designed to provide an accurate chronological framework for the Chusang travertine
102 succession and the human imprints encased in this carbonate (ii) is one of the first studies that focuses
103 on the interplay between thermogene travertine and alluvial/colluvial deposition in a cold-arid
104 periglacial environment and (iii) provides a conceptual model for the relationship between an
105 enhanced summer monsoon and the sedimentary evolution of the Chusang succession.

106

107 **2. Geomorphological setting and basic sedimentary architecture**

108 The Chusang travertine is located near the village of Chusang (variously referred to as Quesang
109 or Qiusang in the literature) about 80 km northwest of the city of Lhasa (Fig. 1). Today, the mean
110 annual air temperature (MAAT) in the study area is $\sim 4^\circ\text{C}$ (derived by adjusting the MAAT of Lhasa to
111 an altitude of 4200 m asl. using the average atmospheric lapse rate of $0.65^\circ\text{C}/100\text{ m}$) and the mean
112 annual precipitation (MAP) is $\sim 430\text{ mm}$ (data from the Public Weather Service Center of China). This
113 part of the Tibetan plateau is under the influence of the Indian and South Asian summer monsoon,
114 delivering ca. 88% of the MAP between June and September (Public Weather Service Center of
115 China).

116 The travertine deposit covers $\sim 0.6\text{ km}^2$ of a gently inclined ($\sim 5\text{-}12^\circ$) NW-facing slope between
117 $\sim 4070\text{ m}$ and 4280 m above sea level (asl.). Two hot springs with a discharge of $\sim 0.1\text{-}0.3\text{ L/s}$ are

118 present at the travertine site (Fig. 1). The main spring is situated at 4270 m asl. and is used in a public
119 bath house (Fig. 1). Steeper slopes are surrounding the travertine and extend up to 4905 m asl..
120 Periglacial slope and mass-wasting processes (frost creep, solifluction) and scarps formed by soil
121 creep and active layer-detachment slides are abundant in the steeper upslope areas above ~4280 m
122 (Figs. 1C, D). A ~560 m-long head scarp is present at the eastern end of the Chusang travertine at an
123 elevation of 4300 m and ~185 m upslope of the main hot spring (Figs. 1C, D). Approximately 1.5 m of
124 displacement and several fresh sinkholes can be observed along this scarp suggesting ongoing
125 subsidence. No additional or superordinate landslides were observed in remote imagery or during the
126 field campaigns at Chusang or in any of the adjacent catchments.

127 Two ephemeral streams incise into the Chusang travertine along its southern and northern margin,
128 respectively (Fig. 1), exposing individual travertine sheets that alternate with layers of colluvial and
129 occasionally alluvial sediment (Figs. 2, 3). Logging along the southern and the northern gully as well
130 as inspection of outcrops along the street reveals at least seven such clastic layers (Fig. 4). Individual
131 travertine beds attain a thickness of 0.3 to 7 m, while layers of clastic sediments vary from 0.5 m to 4
132 m in thickness. The entire thickness of this travertine-colluvium succession is ~24 m. In the upper part
133 of the Chusang travertine (between ~250 m and ~330 m downslope of the modern main spring; Figs.
134 1C, D) at least five paleo-spring orifices, some up to 3 m in diameter and 2 m in height, are located.
135 These orifices represent remnants of former travertine mounds and cones (Figs. 2B, 3A; Pentecost,
136 2005) and occur in the same stratigraphic horizon. Travertine sheets precipitated from water that
137 discharged from these orifices, causing coalescing of the mounds and cones into an interconnected
138 complex (Figs. 1D, 2A). Additional travertine mounds are present at Chusang but are less
139 well-preserved. In south-eastern direction (i.e. upslope towards the human imprints and the modern
140 main hot spring) further layers of travertine and colluvium are overlying this complex with the main
141 modern hot spring discharging on top of this succession (Fig. 2A). Other travertine features such as
142 larger slope terraces, travertine pools or dams are absent. Smaller terraces, mini-rimstone and shallow
143 ponds exist but most of them suffered from surface erosion or are partly covered by clastic sediment.

144

145 **3. Geological setting**

146 The area of Chusang travertine is composed of a sequence of shallow-marine and clastic

147 sedimentary rocks (limestone, sandstone and siltstone), as well as volcanic rocks (tuffaceous rocks,
148 dacite, andesite and lava breccia). This sequence is known as Chaqupu Formation and extends from
149 the Late Paleozoic into the Mesozoic (Zhang, 1997; Xie et al., 2010). Thin-section analysis of a
150 sample obtained from the bedrock that underlies the Chusang travertine at its eastern margin yielded
151 an oolite limestone, which according to Xie et al. (2010) is Triassic in age. The volcanic rocks occur
152 stratigraphically and tectonically below these carbonates and thus likely constitute the deeper parts of
153 the Chusang aquifer (Xie et al., 2010). Tectonically speaking, the study area is part of the Lhasa
154 terrane and situated 27 km east of the Yadong-Gulu graben system (Armijo et al., 1986; Yin and
155 Harrison, 2000), one of six approximately north-south striking graben systems in southern Tibet with a
156 particularly high spreading rate (6.5 mm/yr; Blisniuk et al., 2003; Chen et al., 2004). These grabens in
157 conjunction with normal faults and rifts in northern Tibet and right-lateral strike slip motion along the
158 Yarlung-Tsangbo suture and the Karakorum Jiali fault zone accommodate much of the extensional
159 deformation of the Tibetan plateau that occurred during the Late Cenozoic in response to ongoing
160 north-south shortening of the Tibetan crust and mantle lithosphere (Blisniuk et al., 2001; Taylor et al.,
161 2003; Chen et al., 2004). On the Tibetan plateau, hydrothermal springs are mainly bound to such
162 active extensional faults (Armijo et al., 1986; Ge et al., 2008; Tan et al., 2014). For example, more
163 than two dozens of hot springs and geysers are lined up along the main axis of the Yadong-Gulu
164 graben with several hydrothermal sites – including Chusang – in close proximity to this graben (Han,
165 1981). Based on satellite image studies of lineaments near Chusang village and extensional structures
166 on the travertine itself (both oriented parallel to the Yadong-Gulu graben system; Figs. 1A, B), we
167 assume that the Chusang hot spring, that is situated ~ 27 km east of the graben's main axis, is
168 structurally associated with the Yadong-Gulu graben system.

169

170 **4. Methods**

171 Field investigations were carried out in the summers of 2012 to 2014. Geomorphological
172 mapping in the field was aided by analysis of Google Earth imagery and logging of clastic sediment
173 was based on the lithofacies codes of Eyles et al. (1983). In the field, water temperature, pH, electrical
174 conductivity (EC) and alkalinity of the main and the minor springs were determined in summer 2012.
175 Furthermore, water samples were collected from both springs for chemical analyses. The

176 concentrations of the major cations in the spring water (i.e. Na^+ , K^+ , Ca^{2+} , Mg^{2+} , Sr^{2+}) and Si were
177 determined via inductively-coupled plasma optical emission spectrometry (ICP-OES). Cl^- and SO_4^{2-}
178 concentrations were measured using ion chromatography. The saturation index with respect to calcite
179 (SIcc) of the spring water was calculated using PHREEQC (Parkhurst and Appelo, 1999).

180 This study is based on 25 travertine samples that were cut in half and their macro-fabrics studied.
181 For 20 samples with representative crystal fabrics thin sections were obtained and the position of the
182 most representative samples (i.e. those that are also shown in the Figs. 5-8) are indicated in Figure 1D.
183 Microscopic crystal fabrics were examined under a Nikon Eclipse E400POL microscope using
184 transmitted-light. This microscope is also equipped with an OSRAM HBO mercury short arc lamp to
185 emit light in the UV spectrum (330-380 nm) for epifluorescence microscopy. The mineralogy of 37
186 sub-samples was determined via powder X-ray diffraction (XRD) analyses. Scanning electron
187 microscope (SEM) analyses were performed on polished slabs, with a JEOL JSM-6010LV, operating
188 at 15 kV at a working distance of 21 mm. Furthermore, selected micro-fabrics were analyzed using an
189 electron microprobe (JEOL Superprobe 8100; analytical conditions: 15 kV acceleration voltage and 10
190 nA beam current) in order to (i) determine the elemental content of these fabrics and to (ii) generate
191 elemental concentration maps for selected areas. A micro X-ray fluorescence (μXRF) spectrometer
192 (BRUKER Tornado M4) was used to acquire an element map 20×10 mm (1500×761 pixels) for one
193 of the samples. The μXRF map has a spatial resolution of $13 \mu\text{m}/\text{pixel}$ (equals $>50\%$ beam overlap)
194 and a chemical resolution of ~ 100 ppm.

195 Three samples were sub-sampled for uranium-series (i.e. $^{230}\text{Th}/\text{U}$) dating: two travertine samples
196 (QS-T-6 and P4) and one flowstone-like secondary calcite formed in travertine fracture (sample P6c;
197 Fig. 1D). 5-15 mg calcite powders were obtained from each sample using a hand-held drill and a
198 tungsten carbide drill bit. Chemical separation and purification of U–Th isotopes followed a modified
199 protocols described in Hoffmann (2008). U and Th isotope measurements were undertaken using a
200 ThermoFinnigan Neptune Multi-Collector Inductively Coupled Plasma Mass Spectrometer
201 (MC-ICP-MS) following procedures outlined in Hoffmann et al. (2007). Activity ratios are calculated
202 from isotope concentration ratios using decay constants according to Jaffey et al. 1971 (λ_{238}), Cheng
203 et al., 2000 (λ_{234} and λ_{230}) and Holden 1990 (λ_{232}). The $^{230}\text{Th}/\text{U}$ ages and their uncertainties (quoted
204 at the 95 % confidence level) are given in Table 1.

205

206 **5. Hydrochemistry of the modern hot springs**

207 The main hot spring has a year-round stable temperature of ~ 40-43 °C (Table 1; Tong et al., 2000;
208 Zhang, 1997) with pH values between 6.0 and 6.6 (Table 2). Major ions (100-1000 mg/L) are HCO₃⁻,
209 Ca²⁺, Cl⁻ and Na⁺, whereas Mg²⁺, K⁺ and SO₄²⁻ are present at low concentrations only (<30 mg/L;
210 Table 2). Concentrations of Li, Cs, B and Si were determined too, but only for the main spring, and
211 found to be elevated (Tong et al., 2000; Table 2). The temperature of the minor spring is 23.0 °C, and
212 thus ~19°C lower than that of the main spring (Table 2). Despite this difference in water temperature,
213 the hydrochemistry of both springs is very similar (Table 2). The SIcc values of both springs range
214 from 0.1 to 0.4 (Table 2) and modern carbonate precipitation is restricted to the flow path of the hot
215 spring water, where white carbonate crusts occur that are only a few cm in thickness.

216

217 **6. Mineralogical and elemental composition**

218 XRD and electron microprobe analyses suggest that the dominant mineral of the Chusang
219 travertine is low-Mg calcite (~ 0.2 wt.-% Mg concentration). Aragonite (up ~ 25-50%) was identified
220 in the white pore cement that occurs e.g. in sample QS-T-2A by XRD and electron microprobe
221 mapping (detailed description below). Furthermore, a bulk travertine sample (140 g of sample CS-T-2)
222 was dissolved in hydrochloric acid in order to determine the composition of its insoluble residue. XRD
223 analyses showed that the acid-insoluble residue is composed of quartz, feldspar and mica constituting
224 about ~ 20 wt.-% of the bulk sample.

225

226 **7. Description and interpretation of fabrics and lithofacies**

227 Based on sedimentary logging, the investigation of cut hand specimen and thin-section
228 petrography a range of lithofacies can be recognized within the Chusang travertine-colluvium
229 succession, including (i) a dense laminated, (ii) a porous layered and (iii) a intraclastic travertine
230 lithofacies, as well as (iv) a debris-flow facies comprising colluvial and alluvial sediments. The
231 bedding geometry and thickness along with the (macro- and micro-) fabrics, porosity and diagenetic
232 features that characterize these lithofacies are introduced in the following and summarized in Table 3.

233 **7.1. Dense laminated travertine lithofacies**

234 The dense laminated lithofacies forms lenticular to tabular beds that vary in thickness from 5 to
235 30 cm and are always inclined (~ 5-30 degrees) and mostly dipping downslope (Figs. 3A, C). This
236 lithofacies has low porosity (≤ 5 vol. %) and – on the meso-scale – is characterized by wavy but
237 laterally continuous lamination that is composed of brownish-yellowish laminae (~ 2-4 mm in
238 thickness) that alternate with thin whitish laminae (~ 0.5-1 mm in thickness; Figs. 5A, B).

239 Microscopically, the thick brownish-yellowish laminae are composed of branching calcite
240 crystals that are up to ~ 6 mm long and grew (sub) perpendicularly to the substrate (Figs. 5C, D).
241 These crystals morphologically resemble the “feather dendrites” of Jones and Renaut (1995) or the
242 “cedar-tree crystals” of Kitano (1963) and are thus referred to as dendrites. In many cases dendritic
243 crystals have recrystallized into coarse-grained and bladed spars arranged in a mosaic but the original
244 morphology of the main branches of the former dendrite crystals can still be discerned (Figs. 5C, D).
245 The thin whitish laminae are composed of dark micrite that is usually recrystallized into microsparite
246 (Figs. 5C, D). These microsparitic laminae overlay the dendritic laminae with a sharp contact (Figs.
247 5C, D). Both, the dendritic and micritic laminae lack fluorescence upon UV stimulation.

248

249 *Interpretation*

250 Crystalline dendrites are a common abiotic fabric in travertines and form as a result of fast calcite
251 precipitation from highly supersaturated water driven by rapid degassing of CO₂-rich water (Jones and
252 Renaut 1995; Jones et al., 2000, 2005; Jones and Renaut, 2008). We infer the same mechanism as the
253 main driving force for the formation of the thick dendritic laminae of the dense laminated lithofacies at
254 Chusang. Formation of micrite is commonly associated with microbial mediation, resulting in clotted,
255 peloidal and/or shrub micrites (Chafetz and Folk, 1984; Pedley, 1992; Granding and Cpezzuoli, 2014),
256 but abiotic micrite formation has been reported too (Jones and Renaut, 2008; Jones and Renaut, 2010).
257 The micrite laminae of the dense laminated lithofacies lack biogenic features, both under transmitted
258 light microscopy (Fig. 5) and SEM (SOM 1A-C), suggesting that these micrite laminae might have
259 formed via abiotic processes too. The general lack of-fluorescence in this lithofacies indicates absence
260 of organic compounds, in-line with abiotic calcite precipitation from hot spring water. Both, dendrites
261 and micrite are often affected by early diagenetic alteration, causing partial or complete transformation

262 of dendrites into a mosaic of sparite, while micrite often recrystallized into microsparite (Love and
263 Chafetz, 1988; Jones and Renaut, 2008).

264 In travertines the alternation of dendritic layers with thin micritic bands commonly indicates (i) a
265 seasonal control of travertine growth (e.g. seasonal variation in air temperature) and/or (ii) cyclic
266 changes in flow velocity and flow pattern of the spring water (Jones et al., 2005; Pentecost, 2005;
267 Jones and Renaut, 2008). Based on observations from Clinton travertine in British Columbia (Canada),
268 Jones and Renaut (2008) provide a model of the control mechanism that lead to a dense laminated
269 travertine lithofabric similar to that observed at Chusang: At the Clinton travertine site thick laminae
270 composed of dendrites formed as long as the discharge and the calcite supersaturation are high enough
271 to sustain fast (dendritic) calcite precipitation (i.e. during spring and summer). Strong cooling during
272 winter and/or burial of the spring site beneath ice and snow (at least in the distal parts where the water
273 temperature has cooled down sufficiently) reduced the amount of degassing and decreased the level of
274 supersaturation, thus causing the SI_{cc} to drop below a critical threshold impeding dendritic calcite
275 formation ($SI_{cc} < 2-5$; Jones et al., 2000; Jones and Renaut, 2008). Similarly, snow and ice or partial
276 freezing of spring water will dampen the turbulent nature of the water outflow and also prohibit rapid
277 CO_2 degassing and thus dendritic calcite formation (Jones and Renaut, 2008). According to Jones and
278 Renaut, 2008, thin bands of abiotic micrite – termed growth lines – can form during these seasonal
279 halts of dendrite growth and mark peak winter conditions. In this model the strong seasonality and
280 semi-arid climate is driving the cyclic alternation of dendritic and micritic laminae (in the Clinton
281 region winter temperatures are as low as $-37\text{ }^\circ\text{C}$ and summer temperatures as high as $40\text{ }^\circ\text{C}$; Jones and
282 Renaut, 2008). Similar cyclicity in dendrite growth is also known from the travertine deposits at
283 Lýsuhóll, Iceland (Jones et al., 2005), where, low temperatures in combination with snow and ice
284 accumulation during winter months have been responsible for annual pauses in dendrite growth as
285 well (Jones et al., 2005). The occurrence of growth lines in the dense laminated lithofacies at Chusang
286 (Figs. 5C, D) and the overall similarities to the lithofacies described by Jones and Renaut (2008) and
287 Jones et al. (2005) suggest that this model might also be applicable in a Tibetan context, where winters
288 are known to be particularly cold and dry and summers comparatively mild and wet (winter
289 temperatures at Chusang can attain $-20\text{ }^\circ\text{C}$ and summer temperatures $25\text{ }^\circ\text{C}$; based on data of the
290 Public Weather Service Center of China).

291

292 **7.2. Porous layered travertine lithofacies**

293 High porosity (~20-40%) and cm-scale layering characterize this lithofacies on the meso-scale.
294 The layering is composed of brown porous calcite layers that are ~ 1-2 cm thick and that alternate with
295 yellowish relatively denser calcite layers that are ~ 0.5-1 cm thick (Figs. 6A, B). On the outcrop-scale
296 this lithofacies reveals sub-horizontal tabular bedding with undulated contacts and individual beds that
297 are 10-40 cm in thickness (Fig. 3B). The porous layered travertine lithofacies prevails in the
298 stratigraphically upper section of the Chusang travertine-colluvium succession (0-8 m depth in Fig. 4).

299 Two main types of microscopic crystal fabrics are present in this lithofacies: (1) recrystallized
300 sparite (RSP; Fig. 6D) and (2) dendrites that are recrystallized and preserved as relicts only (relict
301 dendrites – RD; Fig. 6E). The recrystallized sparite is composed of transparent, equant crystals
302 forming mosaics. Such mosaics are common in both, the yellowish dense and the brown porous
303 travertine layers (Fig. 6C; SOM 2A, B). Dark micrite fills most intercrystalline pores (Fig. 6D).
304 Neither the sparites nor the micrite show fluorescence upon UV stimulation. The relict dendrites are
305 confined to the yellowish dense layers and are (i) either recrystallized into a sparite-like mosaic but
306 with the main branches and the first-order sub-branches still preserved (Fig. 6E); or (ii) strongly
307 recrystallized and only the main branches of former dendrites are discernable (Fig. 6D; SOM 2A, B).
308 Originally, none of these dendrites has been longer than ~ 1-2 mm, and most dendrites were even
309 much smaller (~ 200-500 μm). The relict dendrites are sometimes reddish to brownish stained (e.g. Fig.
310 6E), but lack fluorescence.

311 Pores are widespread in the porous layered travertine lithofacies and are mostly 1-10 mm in size.
312 Most pores have irregular shapes, but regular pores that morphologically resemble phyto-moulds and
313 fenestral pores can be observed too and are particularly common in the brown porous layers (Fig. 6C;
314 SOM 2A). Furthermore, evidence of enlargement of these existing pores due to dissolution exists,
315 often blurring the origin of these pores (Fig. 6C; SOM 2A).

316

317 *Interpretation*

318 We invoke abiotic and fast calcite precipitation for the relict dendrites encountered in the
319 yellowish dense layers (Jones et al., 2005; Jones and Renaut, 2008), i.e. the same process as for the
320 dendrites of the dense laminated lithofacies. However, the relict dendrites of the porous layered

321 lithofacies are smaller by an order of magnitude compared to dendrites from the dense laminated
322 lithofacies, suggesting that abiotic calcite precipitation was slower in the porous lithofacies. The lack
323 of fluorescence in the relict dendrites indicates an absence of organic compounds in their crystal lattice,
324 which is in agreement with an abiotic origin of this fabric. Recrystallization (aggrading neomorphism)
325 allowed a sparitic mosaic to form that still resembles the dendritic fabric (Love and Chafetz, 1988;
326 Jones and Renaut, 2008).

327 Compared to the yellowish dense layers the brown porous layers suffered from a higher degree of
328 diagenetic overprinting (recrystallization, dissolution enlargement of pores and precipitation of pore
329 cements). Hence, the formation of these layers is more difficult to decipher, but a biological origin is
330 likely, as outlined in the following. Chafetz and Folk (1984) and Chafetz and Guidry (1999) stated that
331 biological influence becomes significant on travertine precipitation in gradually more distal or lower
332 energy environments. In such distal settings organisms, such as bacteria (particularly cyanobacteria),
333 algae, mosses and reeds can induce and/or influence carbonate precipitation through (i) metabolic
334 process, such as photosynthetic CO₂ removal which increases carbonate saturation and/or (ii) the role
335 played by biofilms and mats as substrates for crystal nucleation (Pentecost, 1995; Fouke et al., 2000;
336 Dupraz et al., 2009; Rainey and Jones, 2009; Fouke, 2011; Della Porta, 2015). Neither
337 transmitted-light microscopy nor SEM analysis on recrystallized sparites of the porous layered
338 travertine lithofacies provide additional clues regarding the importance of biological influence on
339 travertine precipitation. SEM images from the porous layered lithofacies rather confirm that early
340 diagenetic modifications are pervasive and blur the origin of these fabrics (SOM 1D-I).

341 We are thus left with the observations that (i) mouldic pores in travertines as those observed in
342 the porous layered lithofacies are often interpreted as phyto-moulds, i.e. biotic structures that resulted
343 from encrustation and subsequent decay of biological material (e.g. leaves, twigs, weeds, mosses and
344 algae; Heimann and Sass, 1989; Pentecost, 2005); and (ii) fenestral pores are usually caused by the
345 inclusion of gas bubbles but can also be associated with algal mats (Pentecost, 2005).

346 The relatively large size and high concentration of mouldic and fenestral pores in the porous
347 brown travertine layers (Fig. 6C; SOM 2A) suggest that these layers might be associated with
348 enhanced biological activity during the summer months (Heimann and Sass, 1989; Pentecost, 2005;
349 Rainey and Jones, 2009). We envisage that biological material such as algae and other (water) plants
350 acted as nucleation points and/or removed CO₂ via photosynthesis from the water column thus

351 facilitating calcite precipitation, but decayed thereafter, which is in-line with the general lack of
352 fluorescence in the recrystallized sparite that forms the brownish calcite layers. This interpretation is
353 sensible, because during Tibetan summers enhanced monsoon precipitation and higher temperatures
354 stimulate biological activity. Furthermore, mixing of rain and spring water occurs during the summer
355 months as well, thus diluting and cooling hydrothermal water, which in turn favors the growth of biota
356 (Guo and Riding, 1998). We further suggest that the dense yellowish layers that are dominated by
357 relict dendrites represent abiotic travertine precipitation outside the monsoon season (i.e. from October
358 to May). From autumn onward decreasing temperature and increasing dryness slow down or even
359 prohibit mixing of hydrothermal water with rainwater, which in turn slows down and eventually stops
360 organism growth, allowing small abiotic dendrites to form. This process should be particularly
361 important in low-relief areas where ponding of hydrothermal and rain water occurs (Guo and Riding,
362 1998).

363

364 **7.3. Intraclastic travertine lithofacies**

365 This lithofacies forms lenticular to tabular beds with undulating contacts and thicknesses between
366 10 and 40 cm (Fig. 3C). Travertines from this lithofacies contain abundant sand- to gravel-sized (up to
367 20 mm in diameter) intraclasts derived from erosion of pre-existing travertine (Guo and Riding, 1998;
368 Rainey and Jones, 2009; Gandin and Capezzuoli, 2014). These intraclasts are whitish and sometimes
369 brownish in color and most intraclasts are sub-rounded to well-rounded, but sub-angular intraclasts
370 occur as well (e.g. Figs. 7A, B). Also belonging to this lithofacies type are travertine breccia layers (~
371 30-50 cm thick) that are composed of centimeter to decimeter-sized angular travertine clasts (Fig. 3C).
372 These layers are clast-supported and some are blackish in color suggestive of a high organic content
373 and/or the presence of oxidized manganese.

374 On the microscopic scale, the travertine intraclasts are mainly composed of recrystallized sparites
375 (Fig. 7C), but some intraclasts preserve recrystallized dendrites too (Fig. 7D). Most of these intraclasts
376 are surrounded by a thin, irregular dark micrite envelope (Figs. 7C, D). In some samples intraclasts are
377 composed of dark brown micrite and/or microsparite (e.g Fig. 7E). Some of these intraclasts even
378 show a complex internal structure, i.e. consist of multiple calcite clasts, contain calcified bioclasts,
379 show several generations of micrite envelope and/or evidence for dissolution. Only some micritic

380 intraclast as well as the calcified bioclasts show medium to strong fluorescence.

381 Mouldic and fenestral pores with diameters of 0.5-2 mm are present in the intraclastic travertine
382 lithofacies (Figs. 7F, G; SOM 2C). Furthermore, corroded dendrites arranged in a relatively loose
383 network and showing variable growth directions are sometimes preserved and sealed by layers of
384 intraclastic travertine (e.g. sample CS-T-3; Fig. 7H; SOM 2C). In addition, small opaque peloids
385 (50-150 μm in diameter) are present in some samples (e.g. Fig. 7F). These peloids either fill pore
386 spaces or are dispersed in a sparitic carbonate matrix or between micrite clasts and show little
387 fluorescence. Furthermore, pores (including phyto-moulds) are often coated with finely laminated
388 brownish sediment, suggestive of clay coatings (Fig. 7F). Quartz and feldspar grains as well as clay
389 pebbles are present in this lithofacies too, but are not abundant.

390

391 *Interpretation*

392 Several studies have shown that intraclasts in travertines are derived from erosion of lithified
393 travertine deposited in the upstream area and deposition in depressions or ponds (Guo and Riding,
394 1998; Rainey and Jones, 2009; Gandin and Capezzuoli, 2014). Erosion of spring carbonates typically
395 occurs in slope or waterfall settings during high discharge events (Guo and Riding, 1998), but in a cold
396 and periglacial setting such as Chusang frost weathering might also significantly contribute to
397 travertine erosion and thus intraclast formation (cf. Sanders et al., 2010).

398 The sorting of the intraclasts is generally poor in all samples and in combination with the
399 pre-dominant sub-rounded grain morphology this suggests short transport distances. Furthermore,
400 intraclasts with a complex internal structure (dissolution features, several generations of micrite
401 envelopes, composed of multiple intraclasts, contain calcified bioclasts) point towards a complex
402 sedimentation history with multiple cycles of erosion and deposition including dissolution and
403 cementation, at least for some intraclasts. The opaque peloids are most likely organic matter (and
404 possibly contain also manganese oxides; Stoopes, 2003; Rennert et al., 2014) that (i) entered the
405 sediment cascade and were transported and deposited as peloids, or (ii) were washed into the
406 intraclastic travertine at a later stage and filled the pores. Finally, clay infiltrated into these travertine
407 beds, forming laminated pore coatings that also drape opaque peloids.

408 All these micro- and macroscopic observations suggest that the intraclastic travertine lithofacies
409 indicates gentle slopes or distal depressions and/or ponds, where clastic sediment accumulation

410 dominated. The intraclastic lithofacies thus broadly resembles the lithoclastic travertine facies of Guo
411 and Riding (1998). This interpretation is in-line with the observation of corroded dendrites that are
412 arranged in a relatively loose network with variable growth directions and that are overlain by several
413 layers of intraclastic travertine. We interpreted these dendrites as subaqueous in origin, i.e. the
414 expression of a local pond (Fig. 7H; SOM 2C) into which intraclastic travertine was deposited.

415

416 **7.4. Debris flow facies**

417 The sedimentary logs in Figure 4 show that colluvial sediment constitutes a significant proportion
418 of the Chusang deposit (~9.5 m or ~ 40% of the log in Fig. 4). Most of these clastic layers are
419 matrix-supported diamicts, with angular to sub-angular clasts typically up to 20 cm in size embedded
420 in a silt matrix that locally reveals shear planes (Dms; Fig. 4). Some colluvial layers contain abundant
421 (mostly microscopic) organic material (Fig. 3D) and cementation of clastic sediment by carbonate can
422 also be observed (Figs. 3C, 4). One of the thickest colluvial layers (8.4-12 m depth, Fig. 4) reveals an
423 internal sedimentary zonation: greyish sediment that tends to be slightly carbonate-cemented overlays
424 – with an irregular contact – loose brownish slope-wash sediment (Fig. 2B).

425

426 *Interpretation*

427 The matrix-supported diamicts containing angular to sub-angular clasts as well as the presence of
428 shear planes suggest that these clastic sediments are cohesive debris flows sourced from the adjacent
429 hill slopes (Blikra and Nemeč, 1998; Nemeč and Kazancı, 1999). Croci et al. (2016) described
430 colluvial fan deposits interbedded with travertine and concluded that the colluvial fan deposits resulted
431 from debris flows triggered by occasional rainstorms. Significant mass-wasting processes can be
432 expected in a periglacial setting like Chusang, with a catchment reaching in elevation from ~
433 4200-4900 m asl., slopes that are 20°-30° steep and characterized by a sparse vegetation cover and
434 subjected to intensive freeze–thaw weathering (French, 2007). We thus infer that the colluvium
435 interbedded into the travertine is ultimately linked to slope wash and/or periglacial slope processes on
436 the adjacent slopes.

437

438 **7.5. Pore cements**

439 In the dense laminated travertine lithofacies intercrystalline pores and framework pores occur
440 (Fig. 5D), but most of these pores are healed due to widespread recrystallization. In this lithofacies
441 prominent cements only occur in lower stratigraphic positions (i.e. 12-22 m depth; Fig. 4), where they
442 are bound to ~1 mm-thick pores that are up to several centimeters long and extend parallel to the
443 lamination (Fig. 5A). In hand specimens these cements are brown in color (Fig. 5A). Microscopically
444 they are either isopachous (IsoPC; isopachous fibrous or scalenohedral sparitic with thicknesses of
445 100-300 μm ; Fig. 5C) or laminated (LPC, composed of alternating micritic and sparitic laminae, each
446 ~20 μm in thickness; Fig. 5E). Only the laminated pore cement shows bright fluorescence upon UV
447 stimulation (Fig. 5F).

448

449 In the porous layered travertine lithofacies cements are more widespread (particularly in the
450 brown porous layers) and often contain white dense calcite cements that – on the macroscopic scale –
451 are either forming micro-stalactitic crystals that grew downward into the pores (Fig. 6A) or are finely
452 laminated (Fig. 6B). On the microscopic scale at least three types of pore cements are recognized:,
453 fibrous, laminated and dendritic. The same three types of pore cements also occur in the intraclastic
454 travertine lithofacies.

455 The fibrous pore cement (FPC) is composed of large fibrous crystals. These crystals are 0.5-1 mm
456 in length, grew downward into the pore space and reveal an irregular outline (Figs. 6F, G; SOM 2B).
457 The FPC shows undulose extinction under crossed nicols and weak fluorescence (Fig. 6F).

458 The dendritic pore cement (DPC) is dark brownish under transmitted-light and reveal strong
459 fluorescence upon UV stimulation (Figs. 6F, G; SOM 2B). This cement generation either forms a thin
460 (~ 0.1-0.5 mm) veneer covering pre-existing calcite fabrics (e.g. secondary fibrous crystals) or fills
461 pores (Fig. 6F; SOM 2B). The dendritic crystals always grew downward into the pores.

462 The laminated pore cement (LPC) can attain a thicknesses of several mm (Figs. 6B, 8E; SOM 2B)
463 and is composed of translucent sparitic laminae (~ 15-40 μm in thickness) interbedded with thin,
464 brown micrite laminae (~ 5-20 μm ; Fig. 8A). The brown micritic laminae show strong fluorescence,
465 while the sparitic laminae are non-fluorescent (Fig. 8B). This laminated fabric is cross-cut by acicular
466 crystals that are arranged in radiating bundles resembling aragonite (Fig. 8A). In transmitted-light and

477 epifluorescence it can also be observed, that (i) these acicular crystal bundles start radiating from a
478 nucleation point, (ii) the lamination follows the curvature of these bundles, and that (iii) areas
479 composed of laminated fabric only exist as well (Figs. 8A, B). Element mapping reveals that the
480 translucent calcite layers are composed of alternating high and low Mg micro-bands, while the Sr
481 concentration is generally low (Figs. 8C, D). The acicular crystals, in contrast, reveal very low Mg but
482 elevated Sr concentrations (e.g. Figs. 8C, D). The μ XRF analysis show that elevated Sr concentrations
483 (indicative of aragonite) are not uniformly distributed in this pore cement and that the white pore
484 cement is partly Sr-poor (Fig. 8E). Samples for XRD drilled from such areas of laminated pore cement
485 also showed no aragonite.

476

477 *Interpretation*

478 Pore cement in travertines can be directly precipitated by infiltrating spring water, while direct
479 rain and soil-percolation water will preferentially cause surface dissolution and re-precipitation (i.e.
480 karstification; Pentecost, 2005). In many instances mixing of hydrothermal and rain water will occur
481 thus reducing the degree of supersaturation and in combination with the geometry of the pore space
482 determine the type of pore cement. If hot spring water highly supersaturated with respect to calcite
483 percolates the travertine, cement precipitation in the form of dendritic fabrics might be expected.

484 In the dense laminated travertine lithofacies pore cements occur in laterally extensive pore spaces
485 usually confined to the micrite layers. These pores are probably caused by dissolution or fracturing of
486 the laminated travertine, with the micrite layers being a preferential fracture plane or horizon of
487 dissolution. The pores were subsequently filled by isopachous pore cement precipitated under phreatic
488 conditions followed by laminated pore cement that formed under vadose conditions (Figs. 5C, E). The
489 bright fluorescence of the laminated pore cement suggests that this cement precipitated from
490 percolation water that also carried humic and fulvic acids (McGarry and Baker, 2000).

491 In several large pores of the porous layered lithofacies a sequence of at least three cement
492 generations separated by dissolution events can be observed: The oldest cement in the porous layered
493 travertine lithofacies is the fibrous cement that grew from the top of the pores downward and shows
494 clear signs of corrosion (Fig. 6F; SOM 2B). Subsequently, the laminated cement formed, which was
495 affected by corrosion as well (Figs. 6F, 8A, B; SOM 2B). Finally a dendritic cement generation is
496 locally present that covers the fibrous and laminated cements (Fig. 6F; SOM 2B). Particularly bright

497 fluorescence is associated with this youngest cement generation, suggesting that hot spring water
498 containing dissolved humic and fulvic acids infiltrated into the porous travertine deposit during a
499 relatively late diagenetic stage. Continuing hydrothermal activity linked to spatio-temporal variability
500 of hot water flow paths during travertine accretion is a reasonable explanation for repeated infiltration
501 of hydrothermal water into the travertine deposit causing precipitation of dendritic pore cement.

502 An interesting detail of the LPC is that it shows an intergrowth of laminated calcite with acicular
503 crystals. The morphology of these acicular crystals as well as the very low Mg but elevated Sr
504 concentrations measured in these crystals suggest that these needles are composed of aragonite (Figs.
505 8C, D; Pentecost, 2005). XRD analysis conducted on sub-samples taken from this intergrown fabric
506 confirmed the presence of aragonite. XRD analysis from areas that lack such an intergrowth (i.e. are
507 laminated and Sr poor based on μ XRF mapping) yielded calcite but no aragonite. This suggests that in
508 the LPC calcite-aragonite intergrowths and laminated calcite that lacks such intergrowths are
509 co-existing, which is supported by transmitted-light and epifluorescence microscopy (Figs. 8A, B).
510 Furthermore, the fact that the lamination follows the curvature of the aragonite crystal bundles implies
511 that calcite laminae precipitated essentially synchronously with the formation of aragonite crystal
512 bundles (Figs. 8A, B). In sum these observations point towards a co-precipitation of aragonite and
513 calcite rather than diagenetic replacement of aragonite by calcite (Guo and Riding 1992; Folk, 1994;
514 Frisia and Borsato, 2010; see SOM 3 for a discussion of the specific geochemical boundary
515 conditions).

516

517 **8. Discussion**

518 **8.1. Depositional concept and facies model**

519 We synthesize our geomorphological, sedimentological and petrographical observations into a
520 depositional concept and facies model, graphically represented in Figure 9.

521 At 4235 m a.s.l. and 250 m downslope of the modern hot spring a complex of travertine mounds
522 developed on top of a thick colluvial layer that provided a $\sim 10^\circ$ dipping paleo-surface on which the
523 travertine precipitated (Fig. 2B). These mounds are composed of dense laminated travertine (Fig. 3A),
524 and the overall geometry of these mounds is asymmetric (Figs. 9A, B): at the downslope side the
525 travertine dips initially at $\sim 30^\circ$, but after a few meters flattens out and gradually attains the local
526 hillslope angle of $\sim 10^\circ$ (Fig. 2B). The downslope extent of travertine sourced from these orifices can

527 exceed 100 m. Because these mounds form on an inclined surface, accretion against the upper slope is
528 limited by mound height (Figs. 3A, 9B). At Chusang these travertine mounds and slopes are
529 dominated by dense laminated travertine and fit the smooth slope facies of Guo and Riding (1998),
530 where dense crystalline crusts composed of dendritic calcite crystals reflect rapid precipitation under
531 high flow rates.

532 The distal parts of the travertine mounds are dominated by porous travertine of the intraclastic
533 travertine lithofacies and travertine breccia. Dense laminated travertine layers can be intercalated with
534 the intraclastic travertine facies (Fig. 3C). In our depositional model (Fig. 9B) the intraclastic
535 travertine lithofacies results from travertine mound collapse and/or break-up of adjacent travertine
536 slope deposits, while the spring orifices are still active (indicated by the intercalation of dense
537 laminated travertine), resulting in cementation and mixing of intraclastic travertine with in-situ
538 precipitates. This interpretation is in line with sedimentological observations from several other tufa
539 and travertine sites, where erosion and brecciation of travertine slopes and cones caused accumulation
540 of lithoclast travertine at distal slopes and local depressions (Guo and Riding, 1998; Pellicer et al.,
541 2014; Pola et al., 2014). Furthermore, pre-existing colluvium might become partly cemented while
542 travertine mounds are prograding downslope and mixing of intraclastic travertine with colluvium can
543 also occur (Figs. 2B, 3C).

544 While travertine mounds aggragate and eventually combine into larger complexes, flats and local
545 depressions form on top of mounds and behind mound complexes. In our model the growth of
546 travertine mounds on an evenly inclined hillslope mantled with colluvium will thus result in an
547 undulating terrain with areas of low topography that favor ponding. The gentle topography also
548 facilitates the development of the porous layered travertine lithofacies observed at Chusang (Figs. 9A,
549 B) via the following processes: (i) reduced flow velocity of hot spring water that results in
550 precipitation of thin calcite layers composed of small dendrite crystals (i.e. yellow dense layers; Figs.
551 6A, C; SOM 2A), and (ii) dilution of hot spring water by rain water that increases organic growth (e.g.
552 algae, mosses, grasses, etc.) and allows encrustation and biologically influenced travertine
553 precipitation (formation of porous brown layers with mouldic and fenestral pores, Figs. 6A, C; SOM
554 2A). As outlined above, we expect rain water availability and biological productivity, and thus the
555 succession of yellow dense and brown porous calcite layers at Chusang to be mainly controlled by
556 seasonality. According to our depositional model this lithofacies should thus be particularly common

557 in shallow depressions or on gentle slopes where the flow of hot spring water is low and seasonally
558 modulated by rainfall (Fig. 9B) and is broadly comparable to the marsh-pool facies of Guo and Riding
559 (1998). Furthermore, if local growth geometries allow ponds to form that are entirely feed by
560 hydrothermal water with no or only little input of rain or soil-percolation water (at least temporarily),
561 sub-aqueous dendrites develop (Fig. 7H; SOM 2C). Clastic sediment input into these depressions is
562 also common and thus porous layered travertine or subaqueous dendrites are frequently interbedded
563 with colluvium and intraclastic travertine sourced from adjacent hillslopes or travertine mounds (Fig.
564 9B; SOM 2C). Periodically drying of these shallow depressions and gentle slopes results in weathering
565 and staining (sample QS-T-2A, SOM 2B; sample CS-T-3, SOM 2C; Guo and Riding, 1998).

566 Figure 9C depicts a facies succession based on our petrographic observations and the facies
567 distribution model outlined above. In this schematic diagram deposition of dense travertine on a slope
568 or travertine mound grades into porous layered travertine (due to the changing relief while the
569 travertine slope propagates and the mound flattens), followed by the precipitation of subaqueous
570 dendrites (development of local ponds fed by hot spring water behind a growing mound complex) and
571 accumulation of intraclastic travertine (from an adjacent travertine mound and/or hillslope; Fig. 9C).
572 Finally, percolating rain and hot spring waters induce diagenetic alterations, including recrystallization
573 of dendritic fabrics and dissolution of pre-existing travertine and precipitation of pore cements (Fig.
574 9C). The latter process is particularly common in the porous layered travertine lithofacies. The last
575 generation of pore cements of the porous travertine lithofacies is composed of small dendrites,
576 indicating that hot spring water was still flowing from the travertine mounds and (repeatedly?)
577 infiltrated this lithofacies. This observation suggests that travertine formation and early diagenetic
578 alteration (i.e. cementation) can be broadly contemporaneous.

579

580 **8.2. Age constraints and sedimentary evolution**

581 Several aspects of the Chusang travertine render $^{230}\text{Th}/\text{U}$ dating problematic: (i) the widespread
582 recrystallization of primary fabrics likely resulted in open-system behavior and thus gain or loss of
583 radionuclides; (ii) recrystallization might have caused mixing and intermingling of different crystal
584 fabrics of different isotopic composition; and (iii) many calcite samples likely contain unsupported
585 ^{230}Th (i.e. detrital contamination). Given these challenges a precise $^{230}\text{Th}/\text{U}$ chronology will probably
586 not be achievable for the porous layered and clastic travertine lithofacies, where porosity and detrital

587 contamination are high and recrystallization is ubiquitous. Nevertheless, it is expected that careful
588 subsampling of primary fabrics, such as well-preserved dendrites from the dense laminated lithofacies,
589 will yield reliable $^{230}\text{Th}/\text{U}$ dates. In order to obtain a first chronological framework for the
590 colluvium-travertine succession at Chusang we obtained two samples showing well-preserved
591 dendrites from the dense laminated lithofacies from ~7.6 m and ~12.2 m depth (sample P4 and QS-T-6,
592 respectively; Figs. 1D, 4) and one flowstone-like secondary calcite from ~21 m depth that formed in a
593 travertine crack (sample P6c; Figs. 1D, 4). The results are given in Table 1 and suggest that the base of
594 the travertine-colluvium succession has a minimum age that dates into the Middle Pleistocene, while
595 the sample from 7.6 m depth yielded an Early Holocene age.

596 These (preliminary) ages in combination with our facies model provide insights into the
597 sedimentary evolution of the travertine-colluvium succession at Chusang. Travertine spring orifices
598 are known to shift temporally and spatially because travertine cones and mounds frequently self-seal
599 due to the rapid deposition of travertine at the surface or within the throat of hydrothermal spring vents
600 (Pentecost, 2005; Cappezzuoli et al., 2014). Today, the main active hot spring at Chusang emerges at
601 4270 m asl. on top of the travertine-colluvium succession (Figs. 1, 2). The early Holocene travertine
602 sample P4 from 7.6 m depth precipitated from a paleo-spring orifice at ~4212 m asl. that merged with
603 several other travertine mounds and cones that were active at the same time into a laterally extensive
604 travertine sheet (Figs. 2A, B). Older orifices existed further downslope but are morphologically not
605 well preserved; i.e. they must have been situated at ~4113 m asl. ca. 211 ka ago (sample QS-T-6; Fig.
606 2C) and at ~4074 m asl. ca. ≥ 486 ka ago (sample P6c; at the level of the modern Chusang river).
607 These data suggest a lateral shift of the hot spring vent system by ~ 1 km into southeastern direction
608 over the course of the last ca. 500 ka (Fig. 1).

609 A characteristic feature of the Chusang travertine is the interbedding of travertine and colluvium
610 and this interbedding becomes more common in the stratigraphic upper part of the studied succession
611 (Fig. 4). We attribute this general increase of terrigenous sediment input – at least partly – to the fact
612 that the shift of the hot spring vent system towards southeast was also accompanied by (i) vertical
613 aggradation of the travertine deposit and (ii) an increase in the proximity of the hot spring mounds and
614 cones to the nearby hillslopes, which in turn facilitated hill slope processes to interact with
615 hydrothermal carbonate precipitation. The bulk of the colluvium was deposited by cohesive debris
616 flows which sometimes contain organic matter that originates from entrained soil and vegetation of the

617 adjacent hill slopes (Fig. 3D). Because the travertine sheets (particularly the dense laminated
618 lithofacies) are relatively resistant to erosion these sheets also protect the underlying colluvial
619 sediment and thus preserve old terrigenous strata that can contain a biological signal from the former
620 hill slopes.

621

622 **8.3. Paleoclimatic controls**

623 Over centennial to orbital timescales hydrothermal activity and thus travertine deposition is
624 chiefly affected by (i) tectonics allowing hot spring vent systems to open or close and thus influencing
625 deep groundwater circulation (Hancock et al., 1999; Brogi and Capezzuoli, 2009; Brogi et al., 2016) as
626 well as (ii) climate which is a fundamental controlling factor on the hydrology and thus on
627 groundwater recharge (Pentecost, 2005; Viles and Pentecost, 2007). In many instances the
628 development of hydrothermal systems and travertine deposits have been linked to humid climatic
629 phases (Faccenna et al., 2008; De Fillippis et al., 2013; Croci et al., 2016). For the Tibetan plateau it is
630 well established that the Indian summer monsoon (ISM) delivers the bulk of atmospheric precipitation
631 (Tian et al., 2001) and that the intensity of the ISM fluctuated over millennial to orbital timescales in
632 response to insolation changes (Cai et al., 2010, 2015; Zhu et al., 2014; Kathayat et al., 2016). Isotopic
633 studies from Tibet further suggest that (i) hydrothermal spring water is mainly recharged via
634 atmospheric precipitation and that (ii) groundwater circulation on the plateau is rapid and thus
635 residence times for hydrothermal water are short (i.e. a few decades; Tan et al., 2015). For the Tibetan
636 plateau it would thus be reasonable to expect phases of strong ISM and travertine precipitation to be
637 synchronous, albeit the role of tectonics (e.g. earthquake recurrence cycles) has to be considered too
638 (Brogi and Capezzuoli, 2014; Brogi et al., 2014; Gradziński et al., 2014).

639 Climate is also widely recognized as a principal control on colluvial sedimentation, and
640 especially humid climatic conditions (e.g. heavy rainfall) are often triggering debris-flows (Blikra and
641 Nemec, 1998; Nemec and Kazanci, 1999). However, in high-altitude areas an increase in air
642 temperature might induce permafrost degradation and enhance snow-melt runoff and thus also
643 stimulate debris-flow activity (Damm and Felderer, 2013). For Tibet it can be suspected that intensive
644 bedrock weathering of the hillslopes under periglacial conditions (e.g. freeze-thaw cycles) results in a
645 thick slope cover (French, 2007), which in combination with a sparse vegetation cover makes these
646 hillslopes prone to mass-wasting processes. We argue that this preconditioning of the hillslopes in

647 conjunction with an enhanced ISM is likely to cause slope erosion as well as colluvial and alluvial
648 valley aggradation over millennial time scales.

649 Today, no significant debris-flow activity is evident in the Chusang (or in any neighboring)
650 catchment, and erosion is confined to (i) the headward erosion of small gullies and (ii) periglacial
651 slope processes such solifluction, and small-scale active-layer detachment slides at altitudes >4400 m
652 asl (Figs. 1C, D). Modern hot spring activity is similarly sluggish, with very low discharge (~ 0.1-0.3
653 L/s) and only little modern hydrothermal carbonate precipitation. The presence of extensive colluvial
654 sediment layers interbedded with travertine is thus in stark contrast to modern sedimentary processes
655 and hot spring discharge. The sedimentary record at Chusang rather suggests that (i) precipitation of
656 hydrothermal carbonate and erosional processes on the hillslopes were broadly synchronous and (ii)
657 significantly higher in the past (Figs. 4, 9A). We further argue that an enhanced ISM is a plausible
658 driving mechanism for both, travertine precipitation and colluvial sedimentation and thus a possible
659 explanation to reconcile these sedimentological observations.

660

661 **9. Summary and conclusions**

662 The Chusang travertine is a ~24 m-thick sequence composed of hydrothermal carbonate
663 interbedded with colluvium (mainly cohesive debris-flow layers) sourced from the surrounding hill
664 slopes. Geomorphological mapping combined with logging suggests that hot spring water was
665 discharged via travertine mounds onto a ~10° dipping paleo-slope mantled by colluvium. Growth of
666 these travertine mounds is dominated by lateral and downslope progradation, causing individual
667 mounds to merge. This growth mechanism results in an undulating terrain composed of multiple
668 mounds forming a laterally extensive travertine sheet and ultimately controls the occurrence and
669 distribution of the various travertine lithofacies, that include (i) a dense laminated, (ii) a porous
670 layered and (iii) an intraclastic travertine lithofacies. Micro-fabric analyses suggest that the dense
671 laminated travertine lithofacies preserves a cyclic signal that is likely seasonal in nature (i.e. abiotic
672 dendritic calcite precipitation is interrupted during peak winter conditions allowing a thin band of
673 micrite to form). The precipitation of the porous layered travertine lithofacies is cyclic as well and in
674 our interpretation records seasonality via a biologically influenced calcite layer that forms during the
675 monsoon season when both, rainwater availability and temperatures are high, allowing dilution of hot

676 spring water and growth of biota (while abiotic dendritic calcite precipitation dominated during the
677 rest of the year).

678 Diagenesis is ubiquitous in the Chusang travertine, but never alters the original crystal fabrics
679 completely. The most common diagenetic processes include aggrading neomorphism resulting in
680 mosaic-like fabrics composed of recrystallized sparite, and the extensive formation of pore cements
681 that precipitated from infiltrated hot spring and/or rainwater. Most prominent is a generation of white
682 laminated calcite cement that is in parts intergrown with acicular aragonite crystals. Petrographic and
683 geochemical analyses reveal that both polymorphs formed almost coevally and did not suffer from
684 diagenetic alteration.

685 Preliminary $^{230}\text{Th}/\text{U}$ dating suggest that the base of the travertine-colluvium succession at
686 Chusang dates into the Middle Pleistocene, while the top ~8 m of the succession started accumulating
687 in the earliest Holocene. A ~1 km shift of the hot spring orifices from the valley floor into southeastern
688 direction and onto the adjacent hillslopes can be reconstructed from these $^{230}\text{Th}/\text{U}$ data and also
689 explains the general increase of colluvial sediment input into travertine system with time.

690 Today debris flow activity and travertine precipitation are insignificant at Chusang, but the
691 occurrence of large fossil travertine mounds and the interbedding of travertine with thick layers of
692 debris-flows suggests that terrigenous and chemical sediment deposition were (i) orders of magnitudes
693 higher in the past compared to today and (ii) likely synchronous and therefore (iii) probably controlled
694 by the same climatic forcing mechanism. We hypothesize that intervals of strong monsoon enhanced
695 hydrothermal water circulation and travertine precipitation, as well as intensified slope processes and
696 concomitant accumulation of colluvium at hill slope toes.

697 Our study shows that the Chusang travertine-colluvium succession may bear a ~ 500 ka record of
698 paleoclimatic and paleoenvironmental change. Further dating efforts are required to constrain (i) the
699 exact duration of individual pulses of travertine precipitation and colluvial sedimentation, as well (ii)
700 the age for the human imprints encased in the top-most travertine sheet. We suggest that $^{230}\text{Th}/\text{U}$
701 dating of primary dendritic fabrics and of selected clean pore cements and luminescence dating of
702 detrital-rich travertine as well as radiocarbon dating of organic rich colluvium are viable ways forward
703 to obtain a high-resolution record from this unique site. Although likely discontinuous in nature, this
704 sediment succession thus holds the potential to become one of the longest records for Quaternary
705 paleoenvironmental change on the Tibetan Plateau.

706

707 **Acknowledgements**

708 We thank Peter Tropper and Thomas Angerer (University of Innsbruck, Austria) for assistance
709 with microprobe and μ -XRF analyses, respectively. We are grateful to Licheng Shen, Yuchuan Sun,
710 Kunyu Wu and Peng Wang (Southwest University, China) for their field assistance. Diethard Sanders
711 (University of Innsbruck) is thanked for his assistance in petrographic analyses and discussion and
712 Christoph Spötl (University of Innsbruck) for improving a previous version of this paper. We also
713 thank two anonymous reviewers for their constructive comments. This study was supported by the
714 Austrian Science Fund (FWF grant 24924–G19 to MCM) and the Chinese Scholarship Council (CSC
715 fellowship to ZW).

716

717 **Appendix**

718 Supplementary online materials (SOM 1 to 3) is available to this article.

719

720 **References**

- 721 Andrews, J.E., 2006. Palaeoclimatic records from stable isotopes in riverine tufas: Synthesis and review.
722 *Earth-Science Reviews* 75(1-4), 85-104.
- 723 Armijo, R., Tapponnier, P., Mercier, J.L., Han, T.L., 1986. Quaternary extension in southern Tibet - field
724 observations and tectonic implications. *Journal of Geophysical Research-Solid Earth and Planets*
725 91(B14), 13803-13872.
- 726 Ashley, G. M., Dominguez-Rodrigo, M., Bunn, H. T., Mabulla, A. Z. B., Baquedano, E., 2010. Sedimentary
727 geology and human origins: a fresh look at Olduvai Gorge, Tanzania. *Journal of Sedimentary Research*
728 80, 703-709.
- 729 Blisniuk, P. M., Hacker, B. R., Glodny, J., Ratschbacher, L., Bi, S. W., Wu, Z. H., McWilliams, M. O., Calvert,
730 A., 2001. Normal faulting in central Tibet since at least 13.5 Myr ago. *Nature* 412(6847), 628-632.
- 731 Blikra, L.H., Nemeč, W., 1998. Postglacial colluvium in western Norway: depositional processes, facies and
732 palaeoclimatic record. *Sedimentology* 45(5), 909-959.
- 733 Brogi, A., Alçiçek, M. C., Yalçiner, C. Ç., Capezzuoli, E., Liotta, D., Meccheri, M., Rimondi, V., Ruggieri, G.,
734 Gandin, A., Boschi, C., Büyüksaraç, A., Alçiçek, H., Bülbül, A., Baykara, M. O., and Shen, C.-C., 2016,
735 Hydrothermal fluids circulation and travertine deposition in an active tectonic setting: Insights from the
736 Kamara geothermal area (western Anatolia, Turkey). *Tectonophysics* 680, 211-232.
- 737 Brogi, A., Capezzuoli, E., 2009. Travertine deposition and faulting: the fault-related travertine fissure-ridge at
738 Terme S. Giovanni, Rapolano Terme (Italy). *International Journal of Earth Sciences* 98(4), 931-947.
- 739 Brogi, A., Capezzuoli, E., 2014. Earthquake impact on fissure-ridge type travertine deposition. *Geological*
740 *Magazine* 151(6), 1135-1143.
- 741 Brogi, A., Capezzuoli, E., Martini, I., Picozzi, M., Sandrelli, F., 2014. Late Quaternary tectonics in the inner
742 Northern Apennines (Siena Basin, southern Tuscany, Italy) and their seismotectonic implication.
743 *Journal of Geodynamics* 76, 25-45.
- 744 Capezzuoli, E., Gandin, A., Pedley, M., 2014. Decoding tufa and travertine (fresh water carbonates) in the
745 sedimentary record: The state of the art. *Sedimentology* 61(1), 1-21.
- 746 Cai, Y., Cheng, H., An, Z., Edwards, R.L., Wang, X., Tan, L., Wang, J., 2010. Large variations of oxygen
747 isotopes in precipitation over south-central Tibet during Marine Isotope Stage 5. *Geology* 38(3),
748 243-246.
- 749 Cai, Y.J., Fung, I.Y., Edwards, R.L., An, Z.S., Cheng, H., Lee, J.E., Tan, L.C., Sheng, C.C., Wang, X.F., Day, J.A.,
750 Zhou, W.J., Kelly, M.J., Chiang, J.C.H., 2015. Variability of stalagmite-inferred Indian monsoon
751 precipitation over the past 252,000 y. *Proceedings of the National Academy of Sciences of the United*
752 *States of America* 112(10), 2954-2959.
- 753 Chafetz, H.S., Folk, R.L., 1984. Travertines - depositional morphology and the bacterially constructed
754 constituents. *Journal of Sedimentary Petrology* 54(1), 289-316.
- 755 Chafetz, H.S., Guidry, S.A., 1999. Bacterial shrubs, crystal shrubs, and ray-crystal shrubs: bacterial vs. abiotic
756 precipitation. *Sedimentary Geology* 126(1-4): 57-74.
- 757 Chen, Q.Z., Freymueller, J.T., Yang, Z.Q., Xu, C.J., Jiang, W.P., Wang, Q., Liu, J.N., 2004. Spatially variable
758 extension in southern Tibet based on GPS measurements. *Journal of Geophysical Research-Solid Earth*
759 109(B9), doi:10.1029/2002JB002350.
- 760 Cheng, H., Edwards, R.L., Hoff, J., Gallup, C.D., Richards, D.A., Asmerom, Y., 2000. The half-lives of
761 uranium-234 and thorium-230. *Chemical Geology* 169(1-2), 17-33.
- 762 Claes, H., Soete, J., Van Noten, K., El Desouky, H., Marques Erthal, M., Vanhaecke, F., Özkul, M., Swennen, R.,
763 2015. Sedimentology, three-dimensional geobody reconstruction and carbon dioxide origin of

764 Pleistocene travertine deposits in the Ballik area (south-west Turkey). *Sedimentology* 62(5), 1408-1445.

765 Croci, A., Della Porta, G., Capezzuoli, E., 2016. Depositional architecture of a mixed travertine-terrigenous
766 system in a fault-controlled continental extensional basin (Messinian, Southern Tuscany, Central Italy).
767 *Sedimentary Geology* 332, 13-39.

768 Damm, B., Felderer, A. (2013): Impact of atmospheric warming on permafrost degradation and debris flow
769 initiation - a case study from the eastern European Alps. *E&G Quaternary Science Journal* 62/2,
770 136-149.

771 De Filippis, L., Faccenna, C., Billi, A., Anzalone, E., Brilli, M., Soligo, M., Tuccimei, P., 2013. Plateau versus
772 fissure ridge travertines from Quaternary geothermal springs of Italy and Turkey: Interactions and
773 feedbacks between fluid discharge, paleoclimate, and tectonics. *Earth-Science Reviews* 123, 35–52.

774 Della Porta, G., 2015. Carbonate build-ups in lacustrine, hydrothermal and fluvial settings: comparing
775 depositional geometry, fabric types and geochemical signature. *Microbial Carbonates in Space and*
776 *Time: Implications for Global Exploration and Production* 418, 17-68.

777 Dupraz, C., Reid, R.P., Braissant, O., Decho, A.W., Norman, R.S., Visscher, P.T., 2009. Processes of carbonate
778 precipitation in modern microbial mats. *Earth-Science Reviews* 96 (3), 141-162.

779 Eyles, N., Eyles, C.H., Miall, A.D., 1983. Lithofacies types and vertical profile models: an alternative approach
780 to the description and environmental interpretation of glacial diamict and daimictite sequences.
781 *Sedimentology* 30, 393-410.

782 Faccenna, C., Soligo, M., Billi, A., De Filippis, L., Funiciello, R., Rossetti, C., Tuccimei, P., 2008. Late
783 Pleistocene depositional cycles of the Lapis Tiburtinus travertine (Tivoli, Central Italy): possible
784 influence of climate and fault activity. *Global and Planetary Change* 63(4), 299–308.

785 Folk, R.L., 1994. Interaction between bacteria, nanobacteria, and mineral Precipitation in hot-springs of central
786 Italy. *Geographie Physique Et Quaternaire* 48(3), 233-246.

787 Fouke, B.W., 2011. Hot-spring systems geobiology: abiotic and biotic influences on travertine formation at
788 Mammoth Hot Springs, Yellowstone National Park, USA. *Sedimentology* 58(1), 170-219.

789 Fouke, B.W., Farmer, J.D., Des Marais, D.J., Pratt, L., Sturchio, N.C., Burns, P.C. and Discipulo, M.K., 2000.
790 Depositional facies and aqueous-solid geochemistry of travertinedepositing hot springs (Angel Terrace,
791 Mammoth Hot Springs, Yellowstone National Park, USA). *Journal of Sedimentary Research* 70,
792 265–285.

793 Frank, N., Braum, M., Hambach, U., Mangini, A., Wagner, G., 2000. Warm Period Growth of Travertine during
794 the Last Interglaciation in Southern Germany. *Quaternary Research* 54(1), 38-48.

795 French, H.M., 2007. *The Periglacial Environment*. John Wiley & Sons Ltd, Chichester, UK.

796 Gandin, A., Capezzuoli, E., 2014. Travertine: distinctive depositional fabrics of carbonates from thermal spring
797 systems. *Sedimentology* 61, 264–290.

798 Gao, J., Zhou, X., Fang, B., Li, T., Tang, L., 2013. U-series dating of the travertine depositing near the Rongma
799 hot springs in northern Tibet, China, and its paleoclimatic implication. *Quaternary International* 298,
800 98-106.

801 Garnett, E.R., Gilmour, M.A., Rowe, P.J., Andrews, J.E., Preece, R.C., 2004. $^{230}\text{Th}/^{234}\text{U}$ dating of Holocene tufas:
802 Possibilities and problems. *Quaternary Science Reviews* 23(7-8), 947-958.

803 Ge, S., Wu, Q.B., Lu, N., Jiang, G.L., Ball, L., 2008. Groundwater in the Tibet Plateau, western China.
804 *Geophysical Research Letters* 35(18), doi:10.1029/2008GL034809.

805 Gradziński, M., Wróblewski, W., Duliński, M., Hercman, H., 2014. Earthquake-affected development of a
806 travertine ridge. *Sedimentology*, 61(1): 238-263.

807 Grün, R., Schwarcz, H.P., Ford, D.C., Hentzsch, B., 1988. ESR dating of spring deposited travertines.
808 *Quaternary Science Reviews* 7, 429–432.

- 809 Guo, L., Riding, R., 1998. Hot-spring travertine facies and sequences, Late Pleistocene, Rapolano Terme, Italy.
810 Sedimentology 45(1), 163-180.
- 811 Han, T., 1981. Relationship of the active structural system to geothermal activity in southern Xizang (Tibet), in
812 Himalayan Geology II. Geological Press, Beijing, pp. 45-58 (in Chinese).
- 813 Hancock, P.L., Chalmers, R.M.L., Altunel, E., Cakir, Z., 1999. Travertines: using travertines in active fault
814 studies. Journal of Structural Geology 21 (8), 903–916.
- 815 Hill, C. L., 2001. Geological contexts of the Acheulian (Middle Pleistocene) in the Eastern Sahara.
816 Geoarchaeology 16, 65-94.
- 817 Heimann, A., Sass, E., 1989. Travertines in the Northern Hula Valley, Israel. Sedimentology 36(1), 95-108.
- 818 Hoffmann, D.L., 2008. 230Th isotope measurements of femtogram quantities for U-series dating using multi ion
819 counting (MIC) MC-ICPMS. International Journal of Mass Spectrometry 275(1-3), 75-79.
- 820 Hoffmann, D.L., Prytulak, J., Richards, D.A., Elliott, T., Coath, C.D., Smart, P.L., Scholz, D., 2007. Procedures
821 for accurate U and Th isotope measurements by high precision MC-ICPMS. International Journal of
822 Mass Spectrometry 264(2-3), 97-109.
- 823 Holden, N.E., 1990. Total half-lives for selected nuclides. Pure and Applied Chemistry, 62(5), 941-958.
- 824 Jaffey, A.H., Flynn, K.F., Glendenin, L.E., Bentley, W.C., Essling, A.M., 1971. Precision measurement of
825 half-lives and specific activities of ²³⁵U and ²³⁸U. Physical Review C 4(5), 1889-1906.
- 826 Jones, B., Renaut, R.W., 1995. Noncrystallographic calcite dendrites from hot spring deposits in Kenya. Journal
827 of Sedimentary Research 65, 154-169.
- 828 Jones, B., Renaut, R.W., 2008. Cyclic development of large, complex, calcite dendrite crystals in the Clinton
829 travertine, Interior British Columbia, Canada. Sedimentary Geology 203(1-2), 17-35.
- 830 Jones, B., Renaut, R.W., 2010. Calcareous spring deposits in continental settings. In: Alonso-Zarza, A.M., Tanner,
831 L.H. (Eds.), Carbonates in Continental Settings: Geochemistry, Diagenesis and Applications. Elsevier,
832 Amsterdam, pp. 179–214.
- 833 Jones, B., Renaut, R.W., Owen, R.B., Torfason, H., 2005. Growth patterns and implications of complex dendrites
834 in calcite travertines from Lýsuhóll, Snæfellsnes, Iceland. Sedimentology 52(6), 1277-1301.
- 835 Jones, B., Renaut, R.W., Rosen, M.R., 2000. Trigonal dendritic calcite crystals forming from hot spring waters at
836 Waikite, North Island, New Zealand. Journal of Sedimentary Research 70, 586-603.
- 837 Kaiser, K., Schoch, W.H., Mieke, G., 2007. Holocene paleosols and colluvial sediments in Northeast Tibet
838 (Qinghai Province, China): Properties, dating and paleoenvironmental implications. Catena, 69(2),
839 91-102.
- 840 Kaiser, K., Opgenoorth, L., Schoch, W.H., Mieke, G. 2009. Charcoal and fossil wood from palaeosols, sediments
841 and artificial structures indicating Late Holocene woodland decline in southern Tibet (China).
842 Quaternary Science Reviews 28 (15-16), 1539-1554.
- 843 Kitano, Y., 1963. Geochemistry of calcareous deposits found in hot springs. Journal of Science, Nagoya
844 University 11, 68-100.
- 845 Kathayat, G., Cheng, H., Sinha, A., Spotl, C., Edwards, R. L., Zhang, H. W., Li, X. L., Yi, L., Ning, Y. F., Cai, Y.
846 J., Lui, W. G. L., Breitenbach, S. F. M., 2016. Indian monsoon variability on millennial-orbital
847 timescales: Scientific Reports 6, 24374, doi: 10.1038/srep24374.
- 848 Liu, Z.H., Sun, H.L., Lu, B.Y., Liu, X.L., Ye, W.B., Zeng, C., 2010. Wet-dry seasonal variations of
849 hydrochemistry and carbonate precipitation rates in a travertine-depositing canal at Baishuitai, Yunnan,
850 SW China: Implications for the formation of biannual laminae in travertine and for climatic
851 reconstruction. Chemical Geology 273(3-4), 258-266.
- 852 Love, K.M., Chafetz, H.S., 1988. Diagenesis of laminated travertine crusts, Arbuckle Mountains, Oklahoma.
853 Journal of Sedimentary Petrology 58(3), 441-445.

- 854 Mahan, S.A., Miller, D.M., Menges, C.M., Yount, J.C., 2007. Late Quaternary stratigraphy and luminescence
855 geochronology of the northeastern Mojave Desert. *Quaternary international* 166, 61-78.
- 856 Mallick, R., Frank, N., 2002. A new technique for precise uranium-series dating of travertine micro-samples.
857 *Geochimica Et Cosmochimica Acta* 66(24), 4261-4272.
- 858 McGarry, S.F., Baker, A., 2000. Organic acid fluorescence: applications to speleothem palaeoenvironmental
859 reconstruction. *Quaternary Science Reviews* 19(11), 1087-1101.
- 860 Minissale, A., Kerrick, D.M., Magro, G., Murrell, M.T., Paladini, M., Rihs, S., Sturchio, N.C., Tassi, F., Vaselli,
861 O., 2002. Geochemistry of Quaternary travertines in the region north of Rome (Italy): structural,
862 hydrologic and paleoclimatic implications. *Earth and Planetary Science Letters* 203 (2), 709–728.
- 863 Nemec, W., Lonne, I., Blikra, L.H., 1999. The Kregnes moraine in Gauldalen, west-central Norway: anatomy of
864 a Younger Dryas proglacial delta in a palaeofjord basin. *Boreas*, 28(4), 454-476.
- 865 Özkul, M., Gokgoz, A., Kele, S., Baykara, M.O., Shen, C.C., Chang, Y.W., Kaya, A., Hancer, M., Aratman, C.,
866 Akin, T., Özkul, Z., 2014. Sedimentological and geochemical characteristics of a fluvial travertine: A
867 case from the eastern Mediterranean region. *Sedimentology* 61(1), 291-318.
- 868 Özkul, M., Varol, B., Alçiçek, M.C., 2002. Depositional environments and petrography of Denizli travertines.
869 *Bulletin of the Mineral Research and Exploration* 125, 13–29.
- 870 Parkhurst, D.L., Appelo, C.A.J., 2013, Description of input and examples for PHREEQC version 3—A computer
871 program for speciation, batch-reaction, one-dimensional transport, and inverse geochemical calculations:
872 U.S. Geological Survey Techniques and Methods, book 6, chap. A43, 497 p., available only at
873 <http://pubs.usgs.gov/tm/06/a43/>.
- 874 Pedley, M., 1992. Fresh-water (phytoherm) reefs - the role of biofilms and their bearing on marine reef
875 cementation. *Sedimentary Geology* 79 (1-4), 255-274.
- 876 Pellicer, X.M., Linares, R., Gutiérrez, F., Comas, X., Roqué, C., Carbonel, D., Zarroca, M., Rodríguez, J.A.P.,
877 2014. Morpho-stratigraphic characterization of a tufa mound complex in the Spanish Pyrenees using
878 ground penetrating radar and trenching, implications for studies in Mars. *Earth and Planetary Science*
879 *Letters* 388, 197-210.
- 880 Pentecost, A., 1995. The quaternary travertine deposits of Europe and Asia Minor. *Quaternary Science Reviews*
881 14, 1005–1028.
- 882 Pentecost, A., 2005. *Travertine*. Springer, Berlin, 445 pp.
- 883 Pola, M., Gandin, A., Tuccimei, P., Soligo, M., Deiana, R., Fabbri, P., Zampieri, D., 2014. A multidisciplinary
884 approach to understanding carbonate deposition under tectonically controlled hydrothermal circulation:
885 A case study from a recent travertine mound in the Euganean hydrothermal system, northern Italy.
886 *Sedimentology* 61, 172–199.
- 887 Public Weather Service Center of China. Lhasa Climate Normals 1971-2000.
888 <http://www.weather.com.cn/html/cityintro/101140101.shtml>.
- 889 Rainey, D.K., Jones, B., 2009. Abiotic versus biotic controls on the development of the Fairmont Hot Springs
890 carbonate deposit, British Columbia, Canada. *Sedimentology* 56(6), 1832-1857.
- 891 Rennert, T., Händel, M., Höschen, C., Lugmeier, J., Steffen, M., Totsche, K.U., 2014. A NanoSIMS study on the
892 distribution of soil organic matter, iron and manganese in a nodule from a Stagnosol. *European Journal*
893 *of Soil Science* 65, 684–692
- 894 Rich, J., Stokes, S., Wood, W., Bailey, R., 2003. Optical dating of tufa via in situ aeolian sand grains: A case
895 example from the Southern High Plains, USA. *Quaternary Science Reviews* 22(10-13), 1145-1152.
- 896 Sanders, D.G., Ostermann, M., Kramers, J., 2010. Meteoric diagenesis of Quaternary carbonate-rocky talus slope
897 successions (Northern Calcareous Alps, Austria). *Facies* 56(1), 27-46.
- 898 Schulte, L., Julia, R., Burjachs, F., Hilgers, A., 2008. Middle Pleistocene to Holocene geochronology of the

899 River Aguas terrace sequence (Iberian Peninsula): Fluvial response to Mediterranean environmental
900 change. *Geomorphology* 98(1-2), 13-33.

901 Smith, J. R., Giegengack, R., Schwarcz, H. P., 2004. Constraints on Pleistocene pluvial climates through
902 stable-isotope analysis of fossil-spring tufas and associated gastropods, Kharga Oasis, Egypt.
903 *Paleogeography, Paleoclimatology, Paleoecology* 206, 157-175.

904 Smith, J. R., Hawkins, A. L., Asmerom, Y., Polyak, V., Giegengack, R., 2007. New age constraints on the Middle
905 Stone Age occupations of Kharga Oasis, Western Desert, Egypt. *Journal of Human Evolution* 52,
906 690-701.

907 Stone, A.E.C., Viles, H.A., Thomas, L., Van Calsteren, P., 2010. Can ^{234}U - ^{230}Th dating be used to date large
908 semi-arid tufas? Challenges from a study in the Naukluft Mountains, Namibia. *Journal of Quaternary*
909 *Science* 25(8), 1360-1372.

910 Stoops, G. 2003. Guidelines for analysis and description of soil and regolith thin section. Soil Science Society of
911 America, Inc. Madison, Wisconsin, USA.

912 Takashima, C., Kano, A., 2008. Microbial processes forming daily lamination in a stromatolitic travertine.
913 *Sedimentary Geology* 208(3-4): 114-119.

914 Tan, H.B., Zhang, Y.F., Zhang, W.J., Kong, N., Zhang, Q., Huang, J.Z., 2014. Understanding the circulation of
915 geothermal waters in the Tibetan Plateau using oxygen and hydrogen stable isotopes. *Applied*
916 *Geochemistry* 51, 23-32.

917 Taylor, M., Yin, A., Ryerson, F.J., Kapp, P., Ding, L., 2003. Conjugate strike-slip faulting along the
918 Bangong-Nujiang suture zone accommodates coeval east-west extension and north-south shortening in
919 the interior of the Tibetan Plateau. *Tectonics* 22(4), doi:10.1029/2002TC001361.

920 Tian, L.D., Yao, T.D., Numaguti, A., Sun, W.Z., 2001. Stable isotope variations in monsoon precipitation on the
921 Tibetan Plateau. *Journal of the Meteorological Society of Japan* 79(5), 959-966.

922 Toker, E., Kayseri-Özer, M.S., Özkul, M., Kele, S., 2015. Depositional system and palaeoclimatic interpretations
923 of Middle to Late Pleistocene travertines: Kocabaş, Denizli, south-west Turkey. *Sedimentology* 62(5),
924 1360-1383.

925 Tong, W., Liao, Z., Liu, S., Zhang, Z., You, M., Zhang, M., 2000. Thermal springs in Tibet. Science Press,
926 Beijing (in Chinese).

927 Vazquez-Urbez, M., Pardo, G., Arenas, C., Sancho, C., 2011. Fluvial diffidence episodes reflected in the
928 Pleistocene tufa deposits of the River Piedra (Iberian Range, NE Spain). *Geomorphology* 125(1), 1-10.

929 Viles, H., Pentecost, A., 2007. Tufa and travertine. In: Nash, D., McLaren, S. (Eds.), *Geochemical Sediments and*
930 *Landscapes*. Blackwell, Oxford, pp. 173–199.

931 Wang, B.L., French, H.M. 1995. Permafrost on the Tibet Plateau, China. *Quaternary Science Reviews* 14,
932 255-274.

933 Wedepohl, K.H., 1995. The Composition of the Continental-Crust. *Geochimica Et Cosmochimica Acta* 59(7),
934 1217-1232.

935 Xie, Y.W., Liu, H.F., Qiangba, Z.X., Jiang, G.W., 2010. Determination of the formation sequence of Chaqupu
936 Formation of Early-Middle Triassic in the Quesang area, Tibet. *Geological Bulletin of China* 29(12),
937 1833-1839 (in Chinese with English abstract).

938 Yin, A., Harrison, T.M., 2000. Geologic evolution of the Himalayan-Tibetan orogen. *Annual Review of Earth*
939 *and Planetary Sciences* 28, 211-280.

940 Zentmyer, R., Myrow, P.M., Newell, D.L., 2008. Travertine deposits from along the South Tibetan Fault System
941 near Nyalam, Tibet. *Geological Magazine* 145(6), 753-765.

942 Zhang, D.D., 1997. An interpretation of some observations on karst spring regimes and their implication for
943 underground drainage systems in Lhasa karst area, Tibet. *Asian Geographer* 16, 59-71.

- 944 Zhang, D.D., Li, S.H., 2002. Optical dating of Tibetan human hand- and footprints: An implication for the
945 palaeoenvironment of the last glaciation of the Tibetan Plateau. *Geophysical Research Letters* 29(5),
946 1072-1074.
- 947 Zhang, D.D., Li, S.H., He, Y.Q., Li, B.S., 2003. Human settlement of the last glaciation on the Tibetan plateau.
948 *Current Science* 84(5), 701-704.
- 949 Zhao, Y.Y., Cui, Y.B., Zhao, X.T., 2010. Geological and geochemical features and significance of travertine in
950 travertine-island from Zhabuye salt lake, Tibet, China. *Geological Bulletin of China* 29(1), 124-141.
- 951 Zhao, Y.Y., Zhao, X.T., Ma, Z.B., 2006. Study on chronology for hot spring typed Cs-deposit of Targia, Tibet.
952 *Acta Petrologica Sinica* 22(3), 717-724.
- 953 Zhu, L. P., Lu, X. M., Wang, J. B., Peng, P., Kasper, T., Daut, G., Haberzettl, T., Frenzel, P., Li, Q., Yang, R. M.,
954 Schwalb, A., Mausbacher, R., 2015. Climate change on the Tibetan Plateau in response to shifting
955 atmospheric circulation since the LGM: *Scientific Reports* 5, 13318, doi: 10.1038/srep13318.
956

Highlights

A ~24m thick travertine succession interbedded with debris-flow layers occurs in southern Tibet

Depositional model links travertine and concomitant debris flow accumulation

Petrographic analyses suggest seasonal control mechanism on various travertine lithofacies

$^{230}\text{Th}/\text{U}$ ages constrain the lower part of this travertine-colluvium succession to the Middle Pleistocene, top-most ~8 m started accumulating in the earliest Holocene

Fig. 1: Location of the Chusang travertine site (A) and its geomorphological setting (B and C) as well as sampling locations (D). Images B and D are from Google Earth.

Fig. 2: Geomorphological details and sedimentary architecture of the Chusang travertine. (A) View of the stratigraphic upper part of the Chusang travertine-colluvium succession (towards northeast) showing laterally extensive travertine sheets with bathing house complex in the background. (B) View of colluvial layer overlain by a travertine mound complex (southern gully, depth 7-12 m - see Fig. 4; view towards north). The colluvium is composed of greyish (x) and brownish (o) debris-flow deposits. (C) View of the stratigraphic lower part of the succession composed of dense laminated carbonate (bathing house in background marked by an arrow; view towards southeast). Several quarries (Q) indicate mining activities of local population. Sample QS-T-6 was taken from the lower left quarry. Younger alluvial fan sediments that rest on top of travertine are exposed in the foreground.

Fig. 3: Field images showing petrographic characteristics of the Chusang travertine. (A) Paleo-spring orifice ~250 m downslope of the modern main spring with a diameter of ~2 m (red dotted line). Note dense laminated travertine lithofacies dominates the proximal part of travertine mound. (B) The porous layered travertine lithofacies revealing yellowish to reddish surface staining. (C) Middle section of the southern gully (7-10 m depth, see Fig. 4; view towards north) is dominated by a travertine breccia interbedded with dense laminated travertine (10-30 cm in thickness; arrows). Sample P4 was obtained from such a dense laminated travertine layer in this outcrop. (D) Organic-rich colluvial layer overlain by porous travertine.

Fig. 4: Stratigraphic profile for the travertine-colluvium succession at Chuang and position of key-samples and $^{230}\text{Th}/\text{U}$ ages (compare Fig. 1D and Table 1). Note that the key-samples (n = 10, out of a total of 25 samples on which the whole study is based on) are also shown in the Figures 5 to 8. The stratigraphic profile has been compiled from sedimentary logs obtained along erosional gullies that cut into the Chusang travertine (see Fig. 1D for location of gullies).

Fig. 5: Polished slabs (samples QS-T-6 (A) and P4 (B)), and photomicrographs of the dense laminated travertine lithofacies. (A, B) Dense laminated travertines showing lamination that is composed of brownish-yellowish laminae (white arrows) alternating with whitish laminae (black arrows). Note the dark brownish void-filling cement (white open arrows in A) and the reddish (i.e. weathered) laminae in the upper part of B. (C, D) The lamination in both samples QS-T-6 (C) and P4 (D) consists of thick laminae composed of dendrites (RD) that are partly or completely recrystallized to sparite (recrystallized sparite - RSP) and alternate with thin laminae composed of dark micrite (MC). Note the sharp upper contact of the MC laminae to the RSP (arrows in C, D) and isopachous scalenohedral sparitic pore cement (IsoPC in C). (E) Detail of dark brownish and laminated pore cement (LPC; also indicated with white open arrows in A). (F) Strong fluorescence in the LPC (same field of view as E), whereas the IsoPC shows little or no fluorescence. Images C-E taken in plane-polarized light; epifluorescence image F taken under UV stimulation.

Fig. 6: Hand specimen (sample CHU 17(A)), polished slab (sample QS-T-2A (B)) and photomicrographs of the porous layered travertine lithofacies. (A, B) Porous layered travertines showing an alternation of cm-sized brown porous (bp) and yellowish dense (yd) travertine layers. Note the vadose pore cement (PC in A) composed of white fibrous crystals that preferentially occurs in the brown porous layers and an up to 5 mm-thick layer of dense white pore cement that fills a laterally extensive pore (arrow in B). (C) Photomicrograph showing cm-scale alternation of porous and relatively denser travertine layers in sample CHU 17. Dashed lines indicate the layer boundaries. The dense travertine layers are mainly composed of recrystallized sparite (RSP in D), but often preserve relict dendrites (RD in E). The porous layers are characterized by abundant mouldic pores, resembling phyto-moulds and often show evidence for enlargement by dissolution. Note that a few phyto-moulds also occur in the dense calcite layer (C). (F)

Several generations of pore cement occur in the porous layers of sample QS-T-2A, including fibrous pore cement (FPC), laminated pore cement (LPC), and dendritic pore cements (DPC). The FPC consists of large fibrous crystals (D). These fibrous crystals show undulose extinction. The DPC covers the fibrous and laminated pore cements and the growth direction is always oriented downward into the pore space. All cement generations are fluorescent, with the fluorescence signal of the DPC being particularly strong (G). Images C-E taken in plane-polarized light; image F taken in cross-polarized light; epifluorescence image G taken under UV stimulation.

Fig. 7: Polished slabs (sample CS-T-2 (A) and sample CS-T-3 (B)) and photomicrographs of the intraclastic travertine lithofacies. (A) Large whitish sub-round travertine intraclasts (up to 2 cm in size). (B) Small brownish sub-rounded intraclasts (~ 2-5 mm). (C) Detail of a well-rounded intraclast covered by a thin micrite envelope (arrow). This intraclast is composed of recrystallized sparite (RSP), forming an equant mosaic. (D) Detail of a sub-angular intraclast that preserves relict dendrites (RD). Arrow indicates the growth direction of the dendrites. (E) Intraclastic travertine (sample CHU 10) mainly composed of dark, well-rounded micrite intraclasts (0.5-2 mm). Note a large micritic intraclast in lower left-hand corner showing evidence of dissolution (arrows) and containing a large bioclast (circle). (F) Phyto-moulds and brownish clay coatings observed in an intraclastic travertine (sample P1). Note the pore-filling opaque peloids composed of organic matter (om). (G) Mouldic pores surrounded by sparite (circle). (H) Relict dendrites (RD) that are up to several mm in length and show variable growth directions are interpreted as subaqueous in origin (sample CS-T-3, see also SOM 2C). Images C-F taken in plane-polarized light; image G taken in cross-polarized light; image H taken in cross-polarized light and dark field illumination.

Fig. 8: Petrographic details of the laminated pore cement (LPC) in the travertine sample QS-T-2A. (A) Intergrowth of acicular crystals with laminated calcite. The lamination is composed of translucent sparitic layers alternating with brown micrite laminae. The acicular crystals originate from a nucleation point situated in the lower right-hand corner of the image and grew towards the upper left-hand corner of the image forming crystal bundles. Note that the lamination tightly follows the curvature of these aragonite crystal bundles. (B) The acicular crystals showing strong fluorescence. (C, D) Microprobe mapping reveals that the translucent sparitic layers (white rectangle in Figs. C, D) are composed of distinct layers of high (yellow) and low (blue) Mg concentrations. The acicular crystals show very little Mg (dark blue) but elevated Sr concentrations (not shown). (E) The μ XRF analyses confirm the presence of Sr in the LPC (green), but also highlight that Sr is not uniformly distributed in the LPC. Images A and C taken in plain-polarized light; epifluorescence image B taken under UV stimulation; images D and E are the microprobe and the μ XRF mappings, respectively.

Fig. 9: Depositional concept and facies distribution model of the Chusang travertine. (A) Plan view of travertine mounds that merge into mound complexes via lateral and downslope progradation and are influenced by contemporaneous debris-flow activity. (B) Schematic cross section along section A-A' showing the development of travertine mound complexes and the distribution of the travertine facies. (C) Petrographic facies model. For both, the dense laminated and the porous layered lithofacies travertine precipitation is likely controlled by seasonality (for details see text).

Figure 1
[Click here to download high resolution image](#)

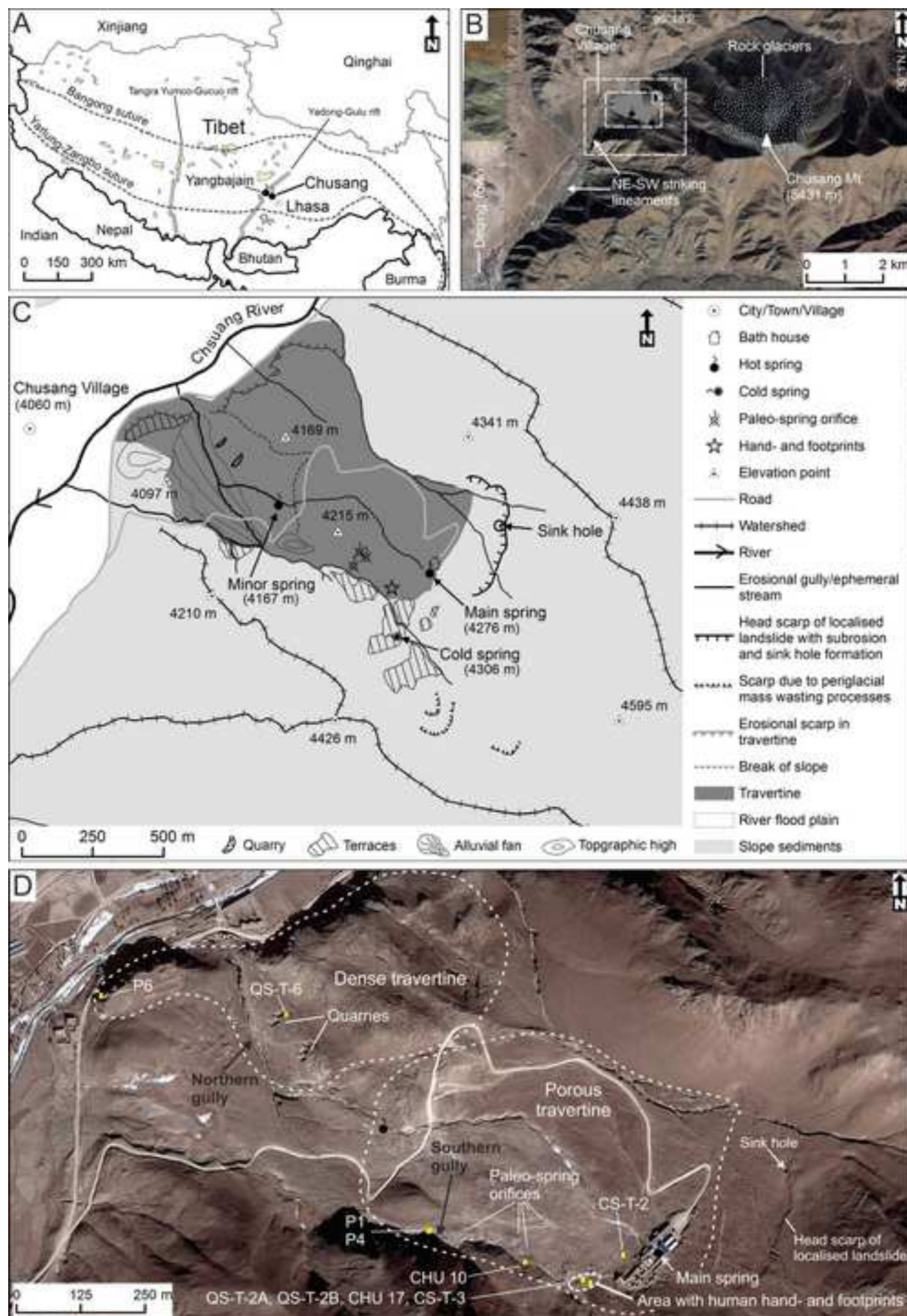


Figure 2

[Click here to download high resolution image](#)

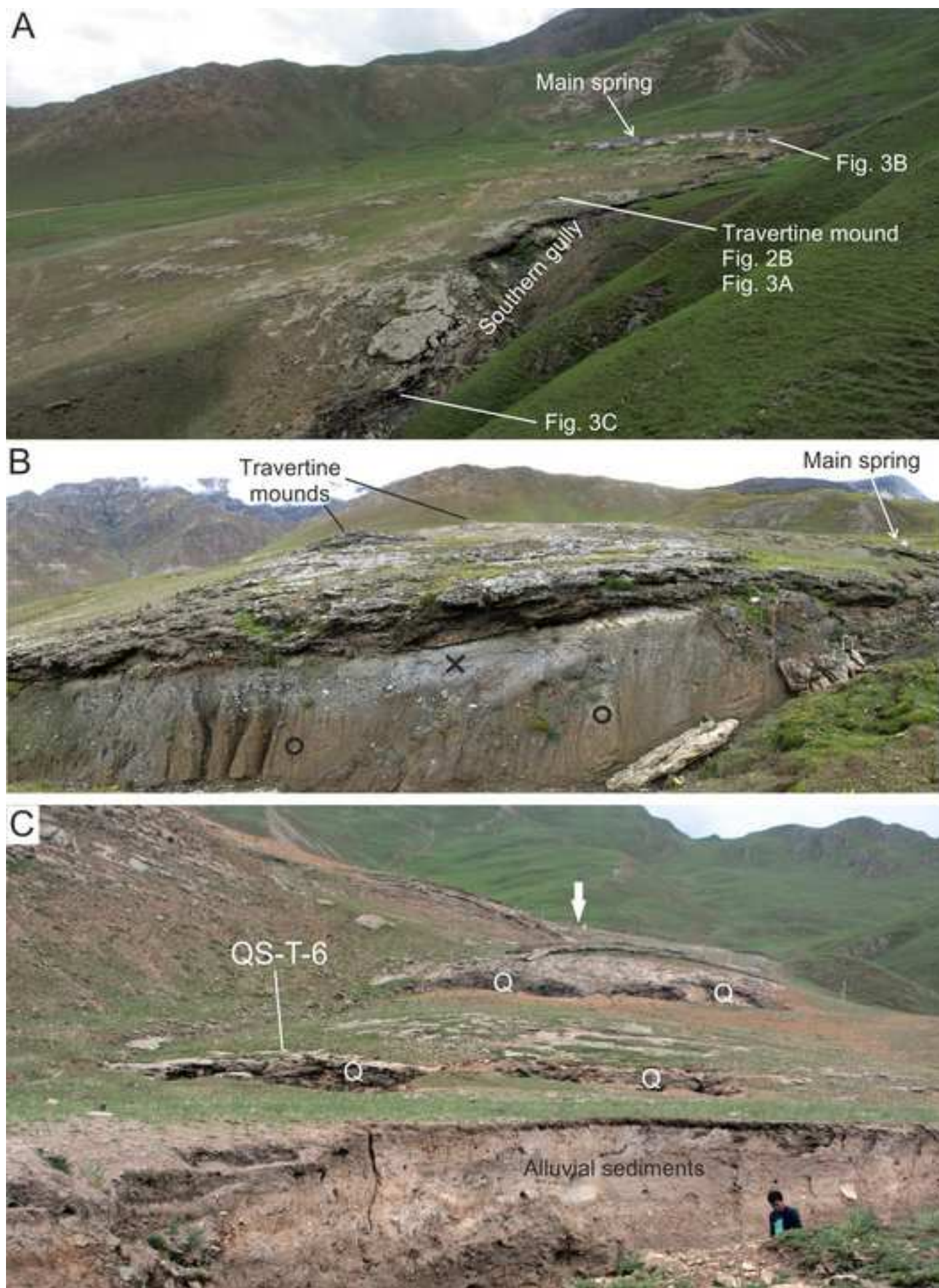


Figure 3
[Click here to download high resolution image](#)

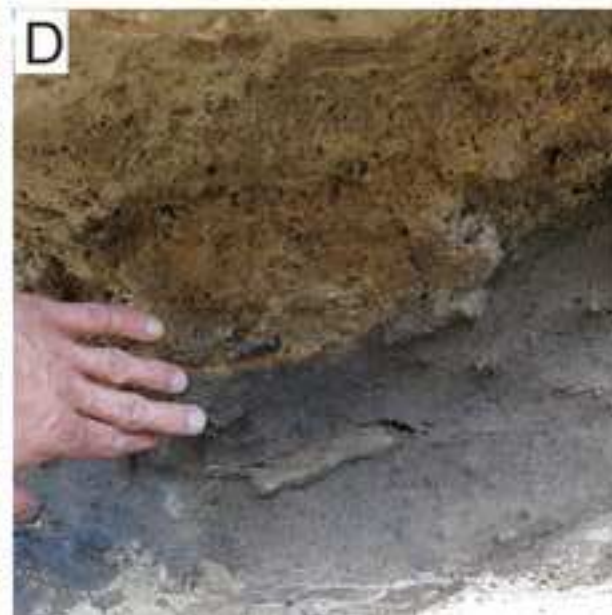
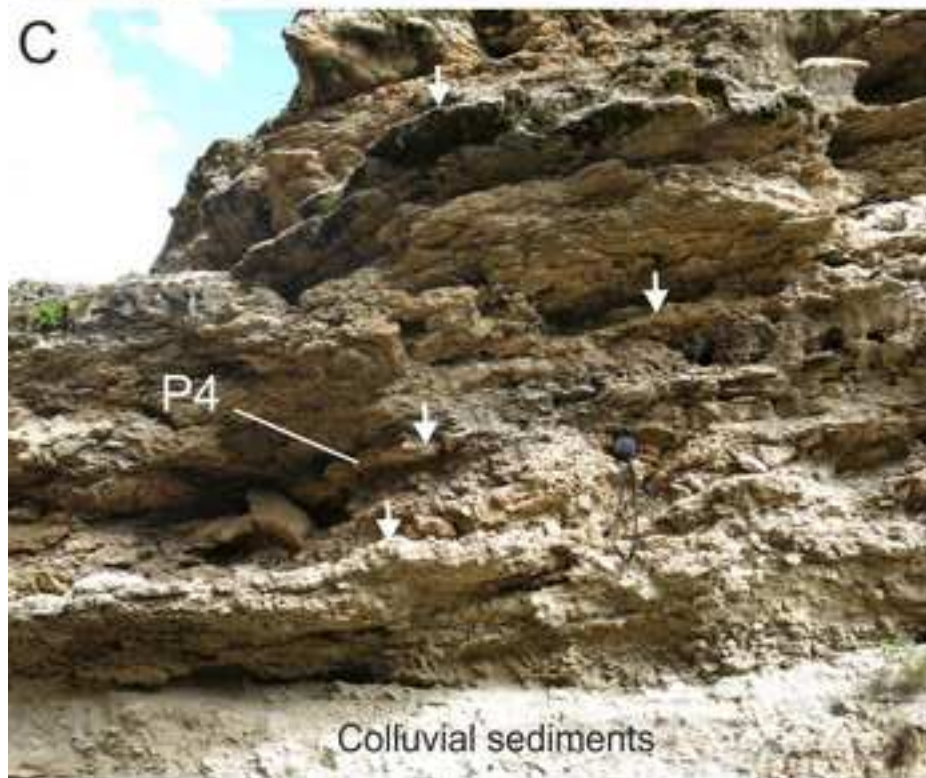


Figure 4

[Click here to download high resolution image](#)

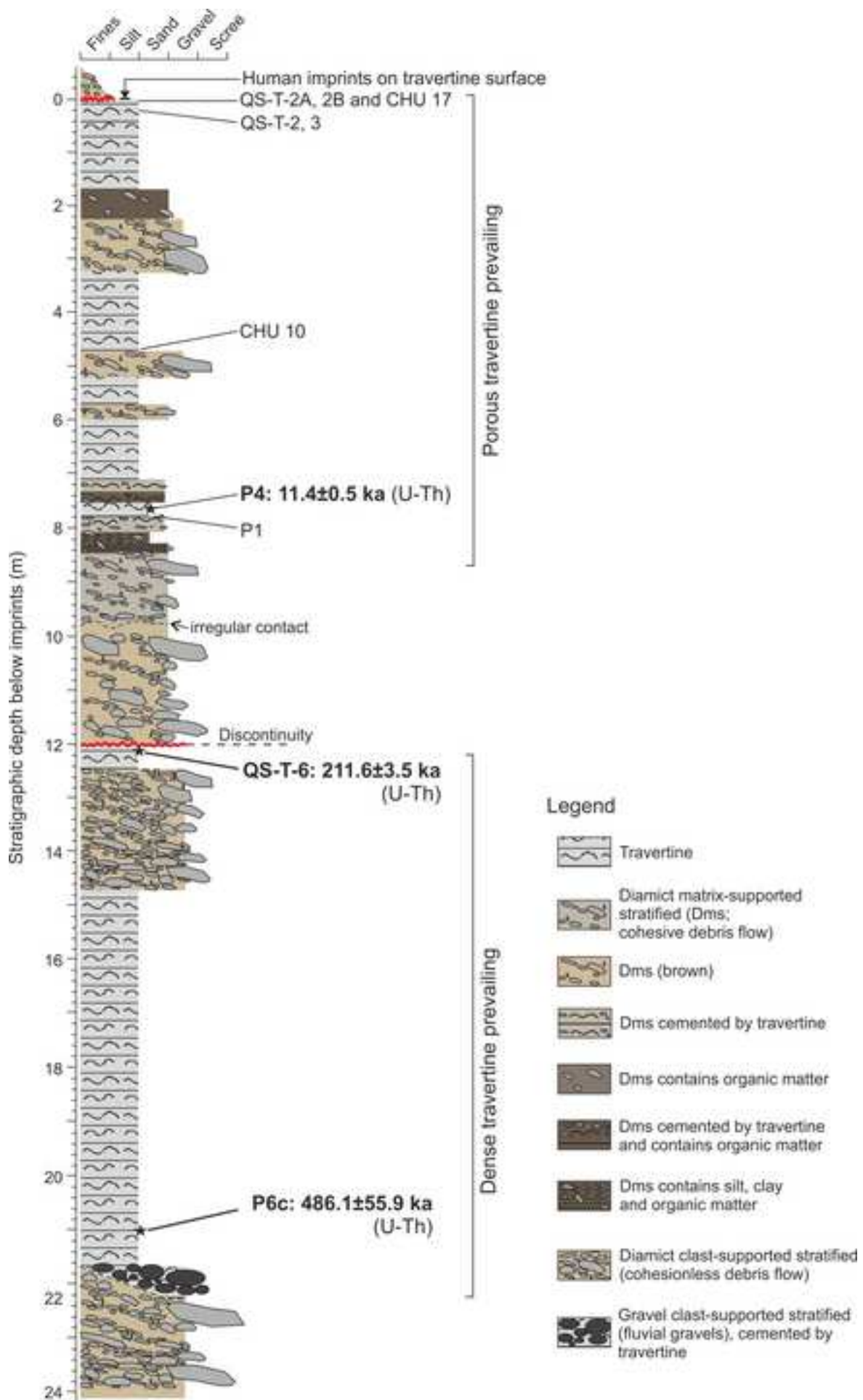


Figure 5
[Click here to download high resolution image](#)

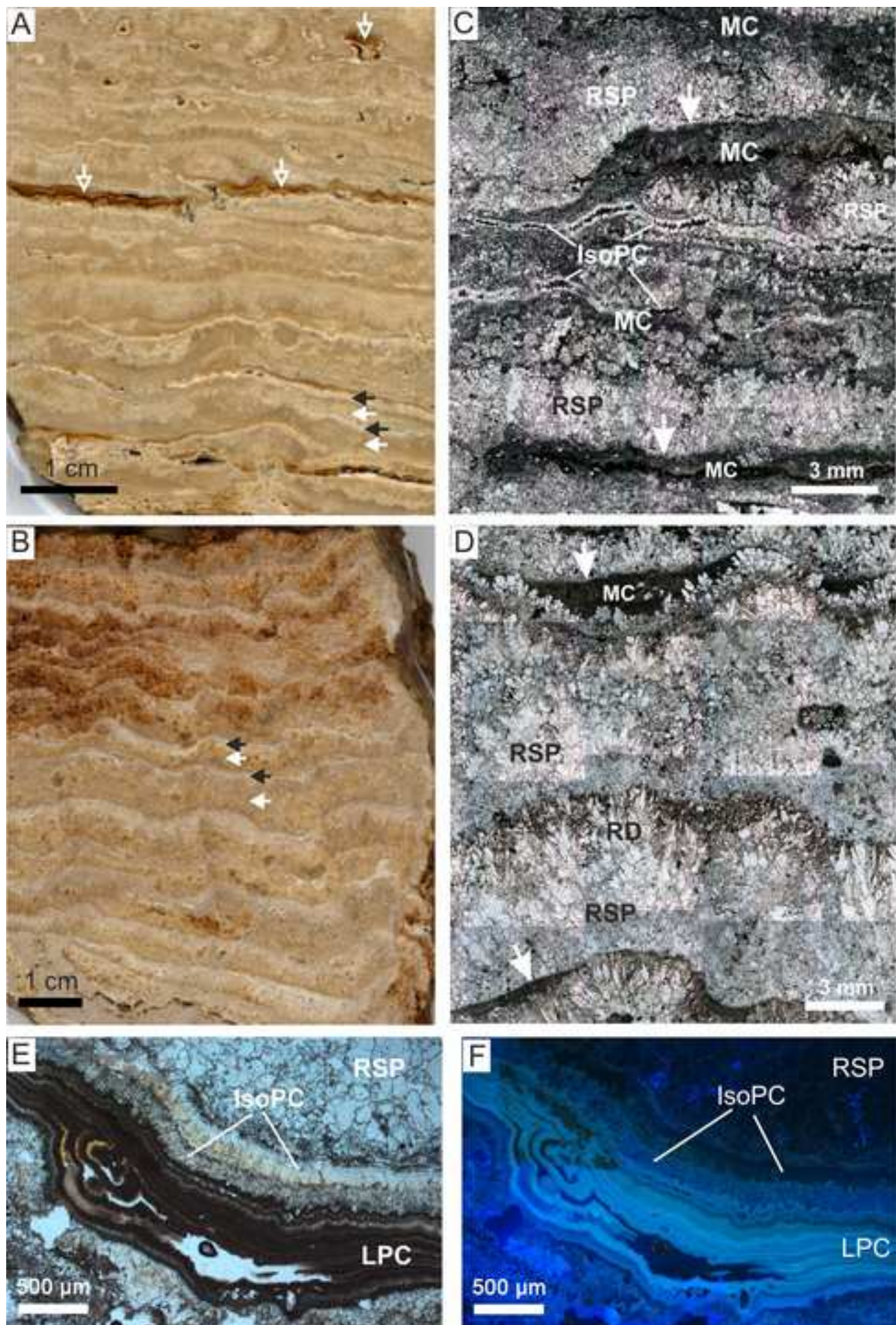


Figure 6
[Click here to download high resolution image](#)

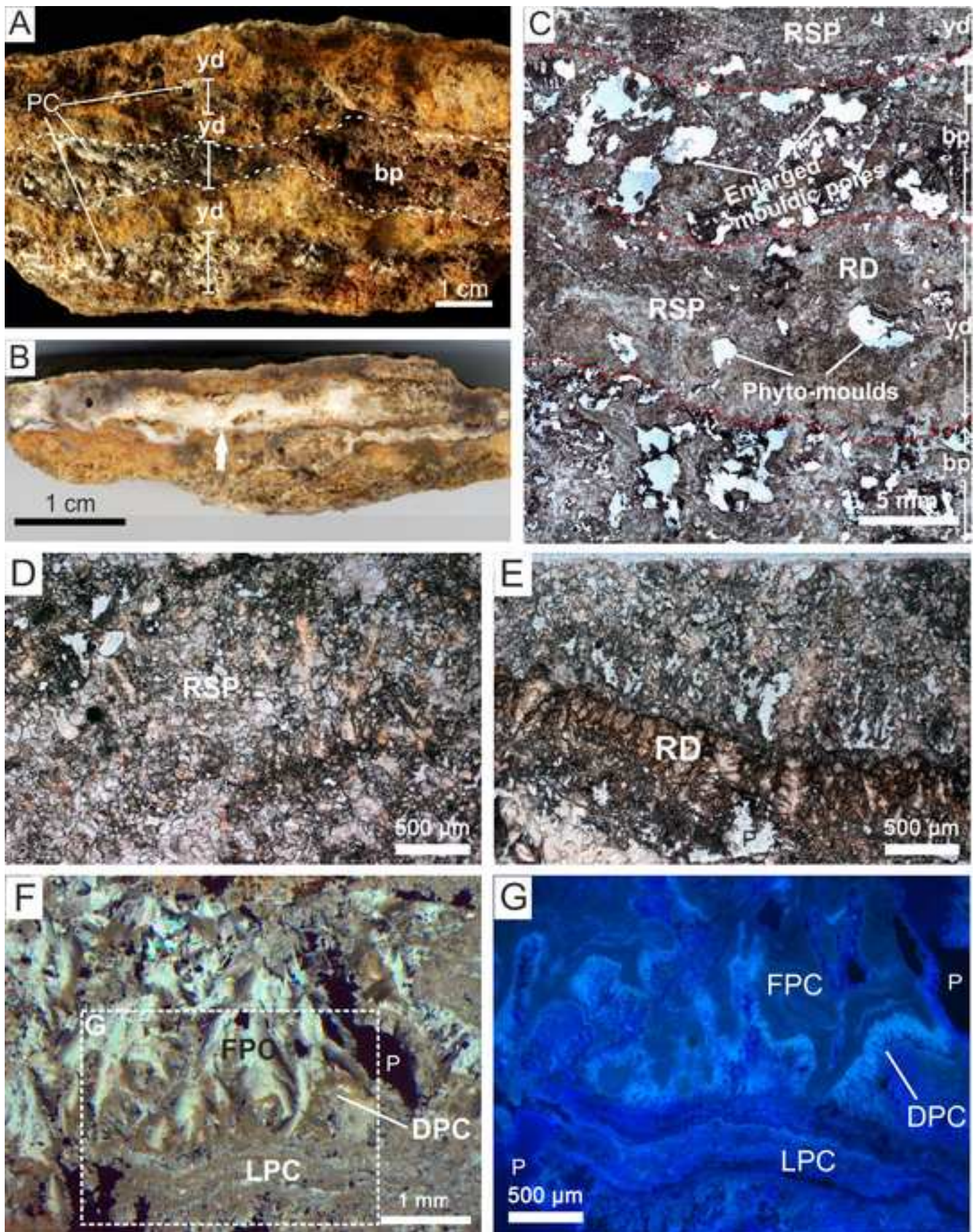


Figure 7
[Click here to download high resolution image](#)

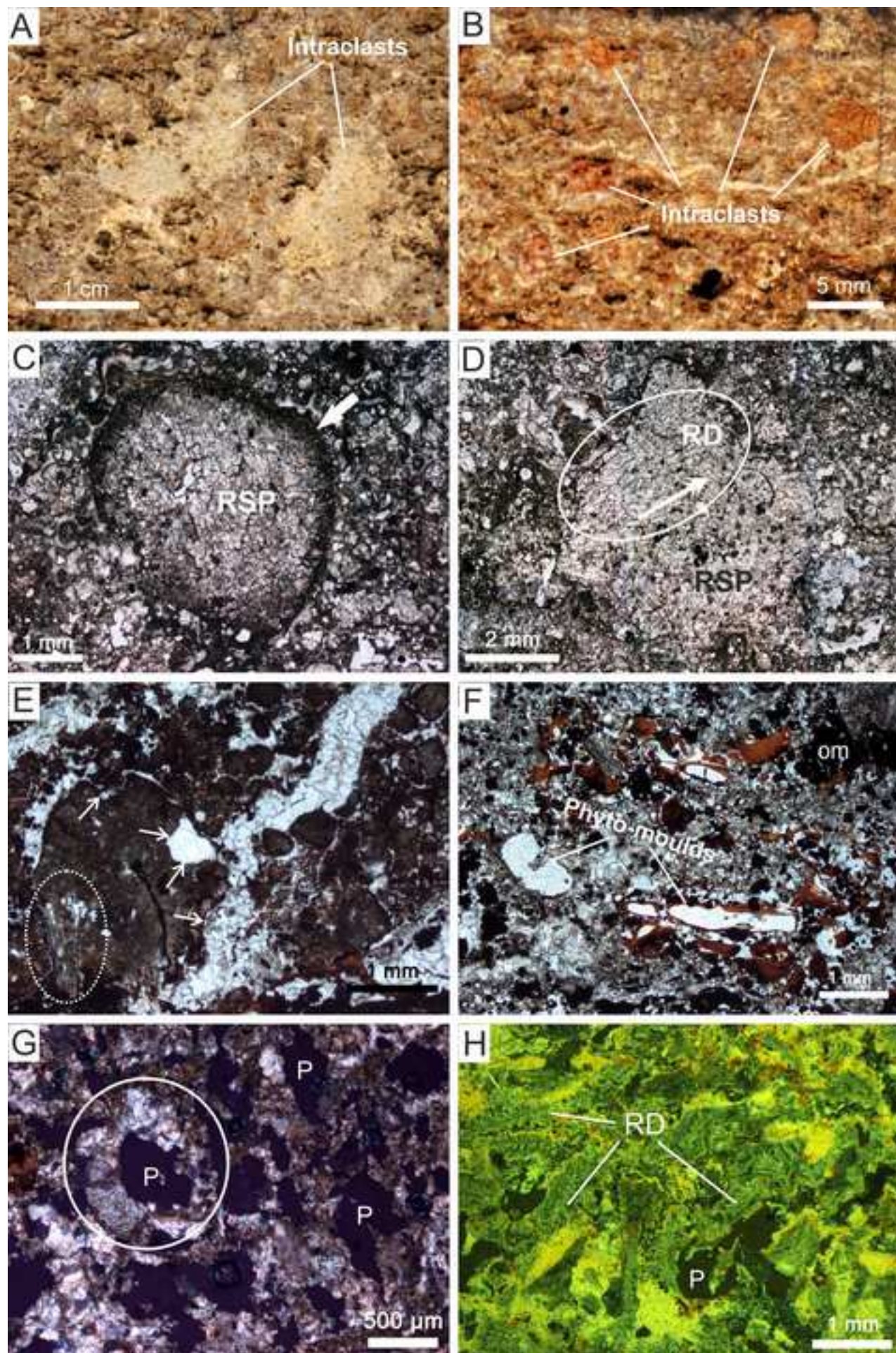


Figure 8
[Click here to download high resolution image](#)

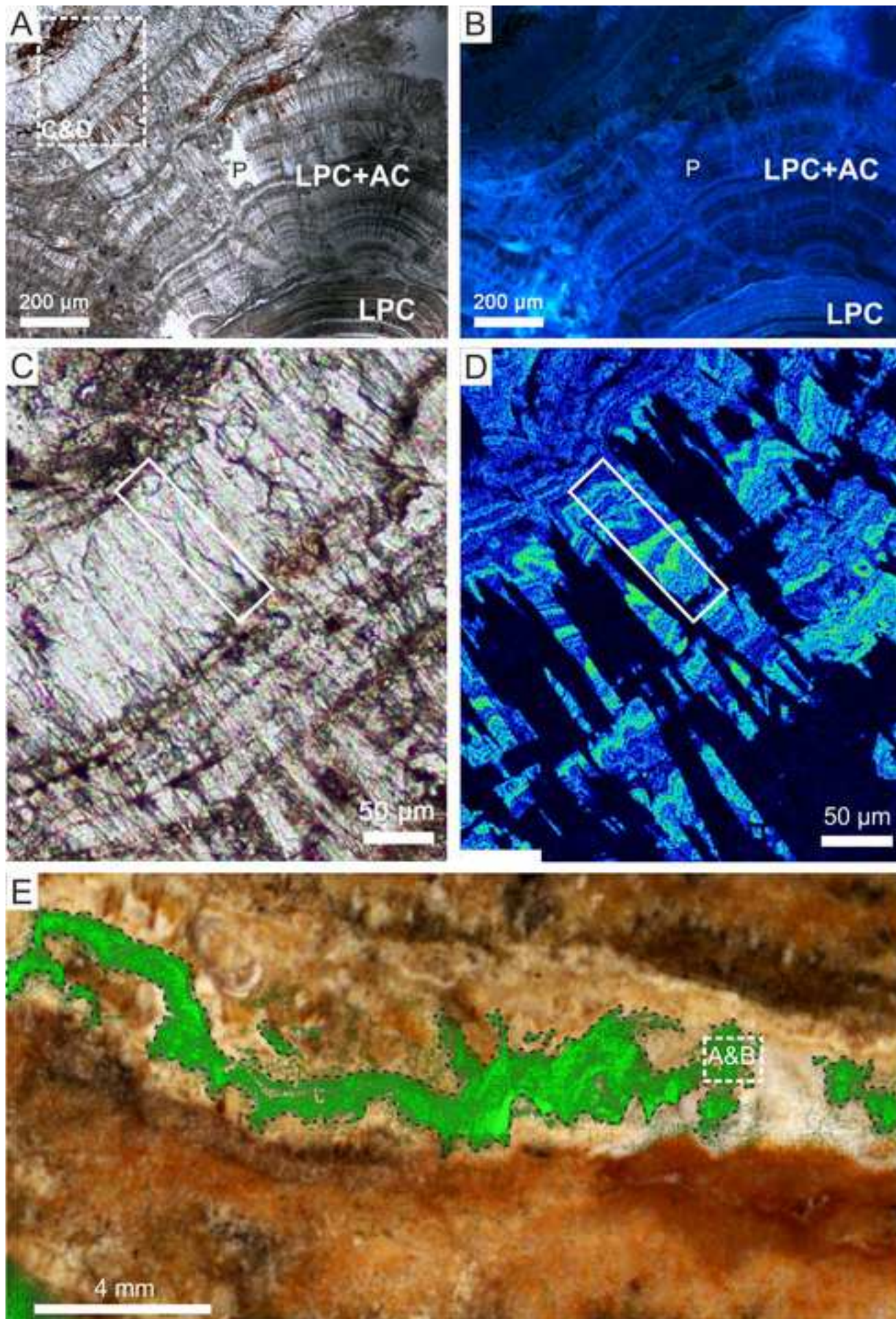


Figure 9

[Click here to download high resolution image](#)

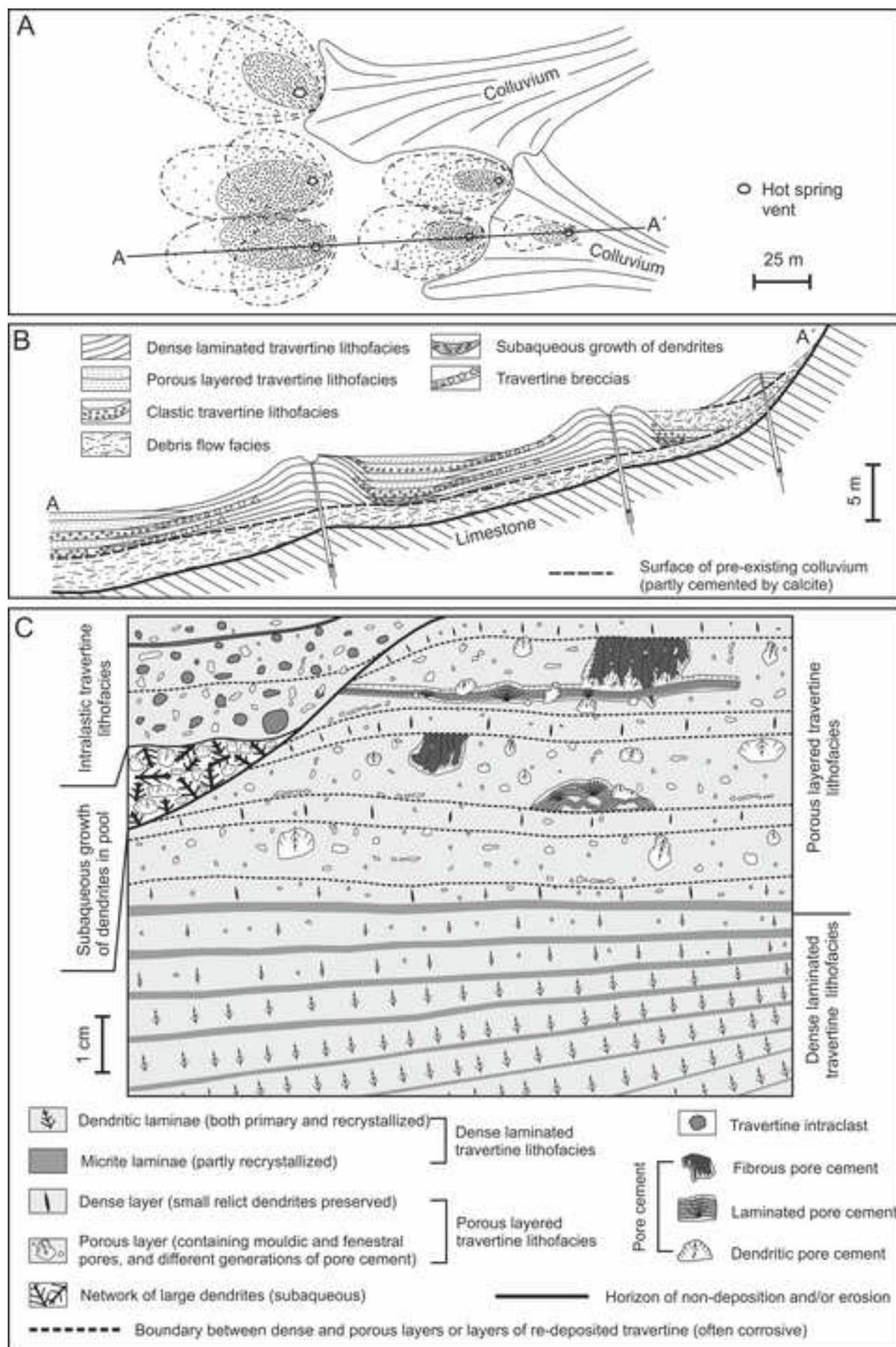


Table 1 Uranium and thorium concentrations, activity ratios and corrected U-Th ages for the Chusang travertine. Corrections for detrital contamination for individual subsamples assumed a value of 0.8 ± 0.4 for the $^{238}\text{U}/^{232}\text{Th}$ activity ratio of the detrital component (Wedepohl, 1995). Uncertainties are reported at the 95% confidence level.

Sample	Fabric	^{238}U	^{232}Th	$[^{230}\text{Th}/^{232}\text{Th}]$	$[^{232}\text{Th}/^{238}\text{U}]$	$[^{230}\text{Th}/^{238}\text{U}]$	$[^{234}\text{U}/^{238}\text{U}]$	Age (ka)	$[^{234}\text{U}/^{238}\text{U}]_{\text{initial}}$
		(ng/g)	(ng/g)	activity ratio	activity ratio	activity ratio	activity ratio	corrected	activity ratio
P4	dendritic	497.59±37.96	35.44±2.69	9.22±0.14	0.02328±0.00005	0.215±0.004	1.985±0.007	11.4±0.5	2.036±0.0122
QS-T-6	dendritic	205.78±3.46	8.47±0.15	80.19±0.54	0.01345±0.00008	1.079±0.005	1.208±0.003	211.6±3.5	1.382±0.0051
P6c	columnar	227.78±2.54	12.08±0.14	59.24±0.27	0.01734±0.00004	1.028±0.005	1.029±0.003	486.1±55.9	1.116±0.0151

Table 2: Chemical compositions of the Chusang hot springs. The data of 1975 and 1989 are from Tong et al. (2000) and Zhang (1997).

	Discharge (L·s ⁻¹)	T (°C)	pH	EC (μS·cm ⁻¹)	Na (mg/l)	K (mg/l)	Ca (mg/l)	Mg (mg/l)	Sr (mg/l)	Li (mg/l)	Cs (mg/l)	Cl ⁻ (mg/l)	SO ₄ ²⁻ (mg/l)	HCO ₃ ⁻ (mg/l)	Si (mg/l)	B (mg/l)	SIcc
Main spring (1975)	1	43.0	6.40	843	135.0	18.8	110.0	21.1	-	1.3	0.8	126.0	21.5	620.0	20.5	13.0	-0.09
Main spring (1989)	0.1	42.2	6.00	927	162.0	28.5	140.0	21.5	-	1.4	2.1	120.0	2.14	635.0	30.8	12.5	-0.40
Main spring (2012)	0.1-0.3	40.0	6.55	1606	142.3	22.4	196.2	21.5	1.7	-	-	148.2	4.0	902.8	16.4	-	0.38
Minor spring (2012)	0.1-0.3	23.0	6.58	1508	138.4	21.6	169.2	23.2	1.7	-	-	130.7	6.2	866.2	16.4	-	0.13

Table 3: Description and interpretation of different lithofacies recognized in the Chusang travertine-colluvium succession.

Lithofacies	Bedding geometry and thickness	Fabrics	Porosity	Diagenetic features	Interpretation of fabrics	Depositional environment and distribution of lithofacies
Dense laminated travertine	lenticular to tabular with sub-parallel contacts; 5-30 cm	<i>dendrites</i> : 1.5-6 mm long, occasionally forming fan-shaped aggregates; <i>micrite</i> : precipitated as thin laminae on top of dendrites partly infilling intercrystalline pores; <i>lamination</i> : 2-4 mm thick dendritic laminae alternate with 0.5-1 mm thin micritic laminae; micritic laminae overlay dendritic laminae with a sharp contact; UV ^a : no fluorescence	≤5 vol. %; <i>intercrystalline pores</i> (0.005-0.5 mm); <i>framework pores</i> (1-2 mm); <i>elongated pores</i> parallel to lamination (≤ 1 mm thick)	<i>recrystallized sparite</i> (RSP): coarse-grained and bladed spars arranged in a mosaic; <i>pore cements</i> : isopachous (IsoPC), laminated (LPC) UV: medium to strong fluorescence for LPC	<i>dendrites</i> : deposited by highly supersaturated hydrothermal water via rapid CO ₂ degassing (i.e. fast abiotic calcite precipitation; Jones et al., 2005); <i>lamination</i> : caused by cyclic (likely seasonal) changes in climate and/or spring discharge rate, <i>micrite laminae</i> interpreted as winter layers (Jones and Renaut, 2008); <i>recrystallized sparite</i> : sparite-like mosaic via aggrading neomorphism (Love and Chafetz, 1988); <i>pore cements</i> : preferential in lower part of the succession (12-22 m depth ^b); precipitated under vadose (LPC) and phreatic (IsoPC) conditions in laterally extensive pores formed by dissolution (Pentecost, 2005);	smooth slopes, relative proximity to travertine mounds and cones; Lithofacies prevails in lower part of the succession (12-22 m depth ^b); interbedded with porous layered and intraclastic travertine
Porous layered travertine	tabular with undulating contacts; 10-40 cm	<i>relict dendrites</i> (RD): ~ 200-500 µm long, prevailing in the dense layers, partly stained; <i>micrite</i> filling intercrystalline pores; <i>layering</i> : ~ 1 to 2 cm thick very porous layers (micritic and/or recrystallized) alternate with ~ 0.5-1 cm thin relatively denser (dendritic) layers; UV: no fluorescence	20-40%; <i>intercrystalline pores</i> (0.005-0.05 mm) <i>mouldic pores</i> (2-10 mm); <i>fenestral pores</i> (0.5-2 mm);	<i>recrystallized sparite</i> (RSP): coarse-grained and bladed spars arranged in a mosaic <i>enlarged pores</i> due to dissolution; <i>pore cements</i> : fibrous (FPC), laminated (LPC) and dendritic (DPC) UV: strong fluorescence for FPC, LPC and DPC	<i>relict dendrites</i> : deposited by supersaturated hydrothermal water via CO ₂ degassing (i.e. slow abiotic calcite precipitation; Jones et al., 2005); <i>recrystallized sparite</i> : sparite-like mosaic via aggrading neomorphism (Love and Chafetz, 1988); <i>mouldic and fenestral pores</i> : dominate in the porous layer, probably result from the decay of e.g. encrusted macrophytes and algal mats (Heimann and Sass, 1989; Pentecost, 2005); <i>porous layers</i> : indicate high biological productivity thus interpreted as summer layers <i>pore cements</i> : mainly precipitated via (re)infiltration of hot spring water and mixing with rain water, vadose conditions (Pentecost, 2005);	low relief topography; lithofacies prevails in the upper part of the succession (0-8 m depth ^b) e.g. in shallow depressions and ponds behind mounds; interbedded with dense and intraclastic travertine
Intraclastic travertine	lenticular to tabular with sub-parallel contacts; 10-50 cm	<i>intraclasts</i> 0.3-20 mm in diameter, sub-angular to well-rounded, composed of recrystallized sparite (RSP), <i>relict dendrites</i> (RD) or micrite and microsparite; thin <i>micrite envelopes</i> surround intraclasts; <i>other allochthones</i> : opaque peloids (0.1-0.4 mm), detrital grains (e.g. quartz, feldspar) <i>travertine breccias</i> : cm to dm, angular clasts UV: no fluorescence, exception: some micritic intraclasts with medium to strong fluorescence	10-20%; <i>intercrystalline pores</i> (0.005-0.05 mm); <i>mouldic</i> and <i>fenestral pores</i> (0.5-2 mm);	<i>recrystallized sparite</i> (RSP): coarse-grained and bladed spars arranged in a mosaic; <i>enlarged pores</i> due to dissolution; <i>pore cements</i> : laminated (LPC), dendritic (DPC); UV: medium to strong fluorescence for LPC and DPC	<i>intraclasts</i> derived from erosion of pre-existing lithified travertine mainly via frost weathering (Sanders et al., 2010); <i>allochthones</i> : input of terrigenous (e.g. quartz, feldspar) and organic matter (organic peloids) e.g. via soil erosion and slope wash processes <i>recrystallized sparite</i> : sparite-like mosaic via aggrading neomorphism (Love and Chafetz, 1988); <i>pore cements</i> mainly precipitated via (re)infiltration of hot spring water and mixing with rain water, vadose conditions (Pentecost, 2005);	distal gentle slopes and depressions/ponds, distal parts of travertine mounds; lithofacies prevails in upper part of the succession (0-8 m depth ^b); interbedded with dense and porous layered travertine
Debris flow	massive layers, no bedding; irregular contacts; 50-300 cm	matrix-supported diamict; (sub-)angular clasts (≤ 20 cm); silty matrix with shear planes; microscopic organic material	n.a.	n.a.	<i>cohesive debris flows</i> caused by soil erosion, slope wash and/or periglacial slope processes (Blikra and Nemeč, 1998; Nemeč and Kazanci, 1999; French, 2007)	proximal to hill slopes, thinning distally; interbedded with travertine (at least 7 colluvial layers ^b)

^a UV: stimulation with UV light (330 – 380 nm; i.e. epifluorescence microscopy)

^b compare Figure 4

SOM 1

[Click here to download Supplementary material for on-line publication only: SOM 1_R1.pdf](#)

SOM 2

[Click here to download Supplementary material for on-line publication only: SOM 2_R1.pdf](#)

SOM 3

[Click here to download Supplementary material for on-line publication only: SOM 3_R1.pdf](#)